

1 **Quantitative evaluation of slip activity in polycrystalline α -titanium considering**
2 **non-local interactions between crystal grains**

3
4 Yoshiki Kawano^{1,a*}, Michihiro Sato^{1,b}, Tsuyoshi Mayama^{2,c},
5 Masatoshi Mitsuhashi^{3,d}, and Shigeto Yamasaki^{3,e}

6
7 ¹Department of Mechanical Engineering, Kitami Institute of Technology, Kitami 090-
8 8507, Japan

9 ²Department of Materials Science and Engineering, Faculty of Engineering, Kumamoto
10 University, Kumamoto 860-8555, Japan

11 ³Department of Advanced Materials Science and Engineering, Faculty of Engineering
12 Sciences, Kyushu University, Fukuoka 816-8580, Japan

13
14 ^a kawano_y@mail.kitami-it.ac.jp

15 ^b sato@newton.mech.kitami-it.ac.jp

16 ^c mayama@kumamoto-u.ac.jp

17 ^d mitsuhashi@kyudai.jp

18 ^e yamasaki.shigeto.259@m.kyushu-u.ac.jp

1 **Abstract**

2

3 An indicator to predict the slip operation at the crystal-grain level, namely slip operation
4 factor (SOF), was established as a function of the Schmid factor (SF) and critical resolved
5 shear stress (CRSS). Plastically “soft” and “hard” regions were estimated by the Schmid
6 factor values normalized by the CRSS—the normalized Schmid factor (NSF). The effect
7 of the interaction among the regions was incorporated into SOF. A microstructural map
8 of α -titanium (α -Ti) was obtained by the electron backscatter diffraction patterns. Several
9 spatial distributions of SOF were calculated based on the map by changing the interaction
10 range among the regions. The distributions were compared with those of the strains
11 obtained by the crystal plasticity finite element (CPFE) analysis. Good agreement
12 between the distributions was found near the macroscopic yield point when the interaction
13 range was appropriate, although some significant differences between the distributions
14 were also noticed after the yielding point. The prediction accuracy by SOF was higher
15 than that by SF and NSF. The reasons for the high accuracy revealed by the SOF analysis
16 and the differences between the distributions indicated by the CPFE analysis were also
17 investigated.

18

19 **Keywords:**

20 Slip operation factor; Schmid factor; Crystal plasticity analysis; Image-based simulation;
21 α -titanium

22

23

24

1 **1. Introduction**

2 **1.1 Need for efficient environment for evaluation of non-uniform deformation**

3

4 The inhomogeneous deformation of metal materials is closely related to the fracture
5 phenomenon, and a lot of studies have been conducted to reveal the relevant mechanisms.

6 Asaro and Rice (1977) reported that in single crystals, work softening for slip systems is
7 not necessary to form strain localization. Peirce et al. (1982) published that geometric
8 softening induced by the crystal lattice rotation with the deformation is an important
9 factor in forming slip bands. As for the polycrystalline materials, the deformation
10 resistance in individual crystal grains varies, while the deformation is inhomogeneous at
11 the beginning. Most metals used as structural materials are polycrystals. As such,
12 understanding the mechanisms of inhomogeneous deformation in the polycrystalline
13 materials leads to safety enhancement and improvements in the performance of many
14 products. The mechanism of inhomogeneous deformation in the polycrystalline materials
15 has been investigated using experimental and numerical methods.

16

17 During the initial stages of deformation in the polycrystalline materials, the anisotropic
18 elasticity of crystal grains induces inhomogeneous deformation (Hook and Hirth, 1967a).

19 When the deformation progresses, the plastic deformation occurs, and the spatial
20 inhomogeneity in strains develops owing to the difference in the deformation resistance
21 and deformation incompatibility among the grains (Bache, 2003; Evans, 1998; Kondou
22 et al., 2008; Kawano et al., 2015; Kawano et al., 2018a). The spatial distributions of
23 crystallographic orientations are required to investigate the mechanisms of
24 inhomogeneous deformation in the elastoplastic ranges at the crystal grain level.

1

2 Both experimental and numerical studies have been conducted to investigate the
3 inhomogeneous deformation of polycrystalline materials depending on their
4 crystallographic orientations. For example, in a number of experimental studies, the
5 relationship between the microstructures with respect to the crystal orientation and slip
6 deformation has been investigated by the X-ray and electron backscatter diffraction
7 (EBSD) patterns (Bridier et al., 2005; Wang et al., 2017; Zhang et al., 2018). In numerical
8 studies, on the other hand, continuum frame work including dislocation theory has been
9 established (Ohashi, 1994; Le and Stumpf, 1996; Ohashi, 1997; Berdichevsky, 2006;
10 Dunne et al., 2007a; Beyerlein and Tomé, 2008; Le and Sembiring, 2008; Langer et al.,
11 2010; Le and Nguyen, 2012; Knezevic et al., 2013; Le and Nguyen, 2013; Le and Günther,
12 2014; Koster et al., 2015; Langer, 2015; Le et al., 2017; Le, 2018). In the conducted
13 numerical studies, crystal plasticity analysis considering such continuum dislocation
14 theory, the slip and twinning deformation modes, or both of them was employed, and the
15 relationship between the microstructures and deformation mechanisms was investigated
16 (Dunne et al., 2007b; Mayama et al., 2011; Roters et al., 2019; Kotha et al., 2019; Kawano
17 et al., 2019a, 2019b). Currently, the crystal plasticity analysis can reproduce various
18 phenomena at the crystal grain level, such as the size effect (Kuroda and Tvergaard, 2006;
19 Ohashi et al., 2007; Le and Sembiring, 2008; Aoyagi et al., 2014; Lewandowski and
20 Stupkiewicz, 2018; Sun et al., 2019), non-Schmid effects (El Kadiri et al., 2013; Cereceda
21 et al., 2016;), temperature dependency and strain rate sensitivity (Lee et al., 2010; Langer,
22 2015; Zhang et al., 2015a; Zhang et al., 2016; Ardeljan et al., 2016; Langer, 2016;
23 Cereceda et al., 2016; Le, 2018; Waheed et al., 2019), Bauschinger effect (Yoshida and
24 Uemori, 2002; Le and Sembiring, 2008; Barlat et al., 2011), development of density in

1 atomic vacancies (Ohashi, 2018; Ohashi and Okuyama, 2019), and growth of voids in the
2 crystal materials (Asim et al., 2019).

3
4 Grain morphology as well as constitutive models affects the deformation mechanism in
5 polycrystalline materials (Zhang et al., 2015b). The crystal plasticity analysis can employ
6 the geometric models built from real microstructures obtained by methods such as EBSD.
7 The spatial distribution of strains obtained by the analysis agrees well with the
8 experimental results (Zhao et al., 2008; Weinberger et al., 2014; Guery et al., 2016a;
9 Zhang et al., 2018; Kawano et al., 2019b). As such, the deformation of polycrystals can
10 be accurately predicted by the crystal plasticity analysis. However, the analysis requires
11 the identification of various physical parameters, and the process of their determination
12 is laborious. Therefore, the development of methods that facilitate the investigation of
13 inhomogeneous deformation mechanisms will lead to the progress of its study.

15 **1.2 Significance of slip deformation indicator and the object of this study**

16
17 The Schmid factor (SF) has often been used as a simple method to predict the slip
18 operation. SF not only characterizes the slip operation, but also represents the ratio of the
19 contribution of the uniaxial stress to the resolved shear stress for each slip system. Thus,
20 when the isotropic elasticity and critical resolved shear stresses (CRSSs) are the same
21 among all of the slip systems, SF can predict the strain distribution at the initial
22 deformation stage with a certain degree of accuracy. However, if the materials possess
23 different CRSSs among the slip systems and anisotropic elasticity (e.g., hexagonal close-
24 packed (HCP) materials with strong anisotropic elasticity), these properties as well as SF

1 affect the mechanism of slip deformation. Moreover, the deformability near the regions
2 of interest affects the deformation in the regions of interest.

3
4 Normalized Schmid factor (NSF) is a type of the Schmid factor normalized by minimum
5 CRSS among the slip systems (Capolungo et al., 2009; Bantounas et al., 2009; Bao et al.,
6 2011). NSF can predict a strain operation more accurately than SF even for materials with
7 different CRSSs among the slip systems. However, the effects of anisotropic elasticity
8 and plastic deformability in the volumes close to the regions of interest are not considered
9 in NSF. Thus, NSF does not fully predict the strain distribution in polycrystalline
10 materials. The aim of this study is to develop an indicator, namely, a slip operation factor
11 (SOF), which accurately and efficiently predicts the strain distribution in such HCP
12 materials with different CRSSs among the slip systems.

13
14 Previous studies have indicated the importance of mechanical interactions among the
15 adjacent “soft” and “hard” grains for the inhomogeneous deformation in HCP materials
16 (Evans, 1998; Bache, 2003; Dunne et al., 2007b; Bieler et al., 2014; Abdolvand et al.,
17 2018). For example, Dunne et al. (2007b) revealed the worst neighbor combination of
18 crystallographic orientations to incur damage under fatigue loading in α -titanium (α -Ti)
19 with the HCP structure. In the inhomogeneous deformation mechanisms, the slip transfer
20 across the grain boundaries is essential (Bieler et al., 2014; Tsuru et al., 2016; Zheng et
21 al., 2017). As such, several indicators to examine the slip transfer were developed (Bieler
22 et al., 2014; Tsuru et al., 2016). Furthermore, an indicator, which is a function of Schmid
23 factor and crystal orientations in adjacent crystal grains, was also developed, and it
24 successfully predicted the strain in Mg alloy (Sun et al., in press). These indicators are

1 the functions of slip strains or values (e.g., the Schmid factor) determined by the crystal
2 orientations. These studies also indicated that the inhomogeneous deformation could be
3 estimated from the distribution of crystal orientations. Mechanical interactions can occur
4 among distant and adjacent grains (Kawano et al., 2019b), and there is a possibility that
5 the prediction accuracy of slip operation increases by considering the effect of the
6 interactions among the distant grains.

7
8 In this study, SOF is formulated and validated. First, we show the formulation of SOF,
9 where a range of the mechanical interactions among the regions is decided arbitrarily.
10 Next, using SOF, we predict the strain distribution of polycrystalline α -Ti, where its
11 microstructure is obtained by EBSD under uniaxial tensile deformation. The strain
12 distribution obtained by the crystal plasticity finite element (CPFE) method is compared
13 with that calculated by SOF. Finally, the accuracy of the prediction of strain distribution
14 is discussed.

2. Formulation of SOF

Let us assume a polycrystalline material under uniaxial tension (Fig. 1). The deformability in region i is determined not only by the softness of the region itself, but also by that of the region surrounding it (Evans, 1998; Bache, 2003; Dunne et al., 2007a; Dunne and Rugg, 2008; Kawano et al., 2018a; Abdolvand et al., 2018). Herein, a novel numerical indicator (SOF) is presented and considers the deformability in the surrounding region to predict the ease of slip operation.

First, normal stress σ in a continuum body under uniaxial tension is applied (Fig. 2). When the plastic deformation occurs in the continuum body by the activation of slip system k , the plastic deformability is determined by the resolved shear stress (RSS) of the slip system. That is, the deformability can be evaluated by SF, which represents the contribution of σ to RSS in slip system k ,

$$m_{SF}^{(k)} = \cos \varphi_1^{(k)} \cos \varphi_2^{(k)}, \quad (1)$$

where $\varphi_1^{(k)}$ is the angle between the loading direction and the vector normal to the slip plane, whereas $\varphi_2^{(k)}$ corresponds to the angle between the loading direction and the vector in the slip direction. When CRSSs among the slip systems are different (e.g., HCP materials), the difference in NSF to evaluate the ease of slip operation has to be considered and is defined as (Capolungo et al., 2009; Bantounas et al., 2009; Bao et al., 2011)

$$m^{(k)} = m_{SF}^{(k)} \cdot \frac{\tau_{CRSS}^{\min}}{\tau_{CRSS}^{(k)}}, \quad (2)$$

2

3 where $\tau_{CRSS}^{(k)}$ is CRSS for slip system k , and τ_{CRSS}^{\min} is minimum CRSS in all of the slip
 4 systems. If the Schmid law is assumed to be proven, the slip deformation operates easier
 5 with higher NSF in the homogeneous stress fields.

6

7 Next, the effect of deformability in the volumes surrounding region i is considered. “Soft”
 8 regions, existing in the loading direction (LD) (Fig. 1b), impede the deformation of region
 9 i because the “soft” regions preferentially deform rather than region i . However, region i
 10 is easier to deform when the “soft” regions exist in the transverse direction (TD) to LD
 11 (Fig. 1c). Indicators \hat{m}_i^{LD} and \hat{m}_i^{TD} need to be defined to consider the effects of relative
 12 softness between regions i and j in LD and TD to predict the ease of slip system operation
 13 as follows:

14

$$\hat{m}_i^{LD} = \sum_{j \neq i} \left[w(\|\mathbf{r}_{ij}\|, r_e^{LD}) \cdot \min \left(\frac{m_i^{\max}}{m_j^{\max}}, R_{\max}^{LD} \right) \cdot |\cos \theta_{ij}| \right], \quad (3)$$

16

$$\hat{m}_i^{TD} = \sum_{j \neq i} \left[w(\|\mathbf{r}_{ij}\|, r_e^{TD}) \cdot \min \left(\frac{m_j^{\max}}{m_i^{\max}}, R_{\max}^{TD} \right) \cdot |\sin \theta_{ij}| \right], \quad (4)$$

18

19 where m_i^{\max} is the maximum value of m' in all of the slip systems, and m_i^{\max} / m_j^{\max}
 20 in Eq. (3) represents the relative ease of slip deformation in region i , in which the value

1 m_i^{\max} / m_j^{\max} is lower when region j is softer. Although m_j^{\max} / m_i^{\max} in Eq. (4) also
2 represents the relative ease of slip deformation in region i , the value m_j^{\max} / m_i^{\max} is
3 higher when region j is softer. R_{\max}^{LD} and R_{\max}^{TD} are the upper limits of these relative
4 values. They prevent the relative values from being excessively large as there should be
5 a limit to the degree of the relative ease of slip operation. θ_{ij} corresponds to the angle
6 that LD makes with direction vector \mathbf{r}_{ij} from region i to j (See Fig. 3a). $|\cos \theta_{ij}|$ and
7 $|\sin \theta_{ij}|$ provide the component of the value in the directions parallel and perpendicular
8 to LD, respectively. w is the weight function that assumes a larger value with closer
9 distance $\|\mathbf{r}_{ij}\|$ between regions i and j . Parameters r_e^{LD} and r_e^{TD} are the effective
10 interaction range between regions i and j in LD and TD, respectively. That is, Eqs. (3) and
11 (4) are calculated by the summation of the relative ease of plastic deformation in LD
12 within the object volume in materials, considering the mechanical interaction among the
13 regions.

14

15 Assuming that the plastic deformability in region i is evaluated by the summation of NSF
16 in region i , and the relative ease of slip operation between regions i and j takes the effect
17 of TD and LD into consideration, the ease of slip operation in region i can be evaluated
18 by

19

$$20 \quad \hat{m}_i = m_i^{\max} + \hat{m}_i^{LD} + \hat{m}_i^{TD}. \quad (5)$$

21

22 Next, \hat{m}_i^{LD} and \hat{m}_i^{TD} in Eq. (5) are normalized using their maximum values to

1 quantitatively evaluate their effect on the ease of slip operation as follows:

2

$$3 \quad \hat{m}_i^{LD} = \frac{\hat{m}_i^{LD}}{\max_{j \in J} [\hat{m}_j^{LD}]}, \quad (6)$$

4

$$5 \quad \hat{m}_i^{TD} = \frac{\hat{m}_i^{TD}}{\max_{j \in J} [\hat{m}_j^{TD}]}, \quad (7)$$

6

7 where J represents the whole regions in the specimen, and \hat{m}_i^{LD} and \hat{m}_i^{TD} are the

8 normalized indicators that consider the effects in LD and TD, respectively, to predict the

9 ease of slip operation. Coefficients A^{LD} and A^{TD} are multiplied by \hat{m}_i^{LD} and \hat{m}_i^{TD} ,

10 respectively, and the resulting values are added to yield SOF as follows:

11

$$12 \quad \hat{m}_i' = m_i^{\max} + A^{LD} \hat{m}_i^{LD} + A^{TD} \hat{m}_i^{TD}. \quad (8)$$

13

14 In Eq. (8), the degree of interaction in LD and TD change with coefficients A^{LD} and

15 A^{TD} , respectively, and the interaction range can be also changed by $w(\|\mathbf{r}_{ij}\|, r_e)$.

16

17 In this study, we employ the following weight function that is typically used in smooth

18 particle hydrodynamics (SPH) which is a type of the particle method (Monaghan, 1988;

19 Müller et al., 2003):

20

$$w(r_{ij}, r_e) = \begin{cases} \frac{315}{64\pi r_e^9} (r_e^2 - \|r_{ij}\|^2)^3, & 0 \leq \|r_{ij}\| \leq r_e \\ 0, & \textit{otherwise} \end{cases} \quad (9)$$

As shown in Fig. 3b, the interaction between the regions is stronger with a closer distance between i and j owing to the effect of w .

In SOF, the ease of slip operation is evaluated by NSF, assuming that the Schmid law is proven. The “relative” ease of slip operation in individual regions is evaluated by the summation of the CRSSs ratio between the regions using Eqs. (3) and (4). As such, the relative ease of slip operation is evaluated based on physics in SOF, and slip operation is likely to occur with higher SOF (although the SOF values do not form a direct connection with the physical values).

3. Prediction of strain distribution by CPFEE analysis

In this study, we compare the SOF spatial distributions and those of strain obtained by the CPFEE analysis to validate SOF. In this section, we present a numerical simulation of uniaxial deformation of polycrystalline α -Ti. A microstructure of the α -Ti specimen was obtained by EBSD. First, we present the CPFEE method. Then, we describe the α -Ti specimen that was employed, the geometric model, and conditions for the analysis. Finally, we reveal the study results.

3.1 Methods of crystal plasticity analysis

A rate-dependent finite-strain crystal plasticity model (Peirce et al., 1983; Asaro and Needleman, 1985) was implemented in this study. The model is described in detail in Appendix. The shear slip rate $\dot{\gamma}$ for slip system k was calculated by

$$\dot{\gamma}^{(k)} = \dot{\gamma}_0 \operatorname{sgn}(\tau^{(k)}) \left| \frac{\tau^{(k)}}{\hat{\tau}^{(k)}} \right|^{\frac{1}{m}}, \quad (10)$$

where $\dot{\gamma}_0$ is the reference shear strain rate for plastic slip, τ is the resolved shear stress (RSS), $\hat{\tau}$ is the reference shear stress, m is the slip rate sensitivity parameter, and $\hat{\tau}$ for slip system k is provided by the Voce hardening law (Voce, 1955; Kocks, 1976) as follows:

$$\hat{\tau}^{(k)} = \tau_0^{(k)} + (\tau_1^{(k)} + \theta_1^{(k)} \gamma) \left\{ 1 - \exp\left(-\frac{\theta_0^{(k)} \gamma}{\tau_1^{(\alpha)}}\right) \right\}, \quad (11)$$

2

3 where τ_0 , τ_1 , θ_0 , and θ_1 are the parameters to represent the relationship between the
 4 shear stress and shear strain.

5

6 **3.2 Sample material and geometric model**

7

8 The chemical composition of the test material employed in this study is summarized in
 9 Table 1. The processing sequence used for the test material was hot and cold rolling with
 10 heat treatment for 2 h at 650 °C for the microstructure homogenization. The EBSD crystal
 11 orientation map was obtained from the test material (Fig. 4a). The geometric model for
 12 the numerical analyses (Fig. 4b) was built from the map using the data conversion system
 13 developed by Kawano et al. (2018b).

14

15 **3.3 Conditions for CPFЕ analysis**

16

17 The uniaxial loading was applied to the geometric model. Fig. 4b demonstrates the surface
 18 on the left side that is fixed in the X-direction with the forced displacement applied to the
 19 surface on the right side. Zero stress was applied to other surfaces. In this study, we
 20 analyze the inhomogeneous strain distribution at the initial deformation stage. The
 21 important physical parameters at the initial deformation stage typically constitute the
 22 elastic compliance and CRSS. The elastic compliances of pure Ti (Fisher and Renken,
 23 1964) were employed (Table 2). To investigate the effect of anisotropic elasticity on the

1 strain distribution, the isotropic elasticity condition with the Poisson's ratio ($E = 106.3$
 2 GPa) and Young's modulus ($\nu = 0.34$) from polycrystalline CP-Ti was also applied (Hook
 3 and Hirth, 1967a; Kondou et al., 2008; Mayama et al., 2009; Kawano et al., 2015; Tada
 4 and Uemori, 2018; Kawano et al., 2018a). The slip systems are assumed to be basal,
 5 prismatic $\langle a \rangle$, pyramidal $\langle a \rangle$, and 1st- and 2nd-pyramidal $\langle c+a \rangle$ (Fig. 5). The CRSSs are
 6 determined by parameter $\hat{\tau}^{(\alpha)}$ in Eq. 11. The parameters used in Eq. (11) are shown in
 7 Table 3, which are determined based on CRSS of α -Ti as estimated by Pagan et al. (2017),
 8 although the CRSS values of α -Ti differ depending on the study (Conrad, 1981; Philippe
 9 et al., 1995; Wu et al., 2007; Warwick et al., 2012; Benmhenni et al., 2013; Hama et al.,
 10 2017; Pagan et al., 2017). The $\hat{\tau}^{(\alpha)}$ value changes as a function of slip strain (Fig. 6).
 11 Work softening on each slip system in α -Ti (Pagan et al., 2017; Wang et al., 2017) was
 12 not taken into consideration. The material employed in this study was polycrystalline α -
 13 Ti with a single phase and large grain size (average grain size $D_{ave} = 69.2 \mu\text{m}$). The
 14 effects of size (Okazaki and Conrad, 1972; Sergueeva et al., 2001) and the second phase
 15 (Radecka et al., 2016) were ignored in the current CPFEM analysis. The occurrence of
 16 twinning commonly decreases with increasing concentrations of oxygen (O) and
 17 aluminum (Al) (Hanada, 1990; Lütjering and Williams, 2007; Fitzner et al., 2016).
 18 Although the O and Al contents were low in the test material employed in this study
 19 (Table 1), twinning was ignored for the sake of simplicity. As shown in τ_0 in Table 3,
 20 the magnitude relation of initial CRSSs among the slip systems is as follows: prismatic
 21 $\langle a \rangle < \text{basal} < 1^{\text{st}} \text{ pyramidal} \langle a \rangle < 1^{\text{st}} \text{ and } 2^{\text{nd}} \text{ pyramidal} \langle c+a \rangle$. The strain rate was
 22 assumed to be 1.0×10^{-3} . The slip rate sensitivity parameter $m = 0.02$ was employed
 23 (Hasija et al., 2003; Hama et al., 2017).

3.4 Strain distribution predicted by CPFE analysis

The spatial distributions of normal strain ε_{XX} in the X (loading)-direction are presented in Fig. 7a, and the relationship between the average normal stress and strain are shown in Fig. 7b. The distribution of ε_{XX} is inhomogeneous around the yield point ($\overline{\varepsilon_{XX}} = 0.006$), and the inhomogeneity increases with the deformation ($\overline{\varepsilon_{XX}} = 0.031$). The distributions of slip strain (γ) obtained during the same analysis are displayed in Fig. 8. The distributions of slip strain (γ_{total}) correspond well with those of ε_{XX} . That is, the slip strain determines the distribution of ε_{XX} after the yielding in this analysis. In addition, the slip strain in the primary slip system (γ_{basal}) is dominant around the yielding point, and the distribution is similar to that of ε_{XX} due to the small elastic deformation. In contrast, the activation of the secondary slip systems makes a difference between the distributions of γ_{basal} and ε_{XX} as the deformation progresses. The inhomogeneous strain distributions observed in the current analysis reflect the low work-hardening rate of the primary slip system in α -Ti. When the work-hardening rate is higher due to the effect of the second phase (Radecka et al., 2016), the strain distributions become more homogeneous, and the secondary slip systems may activate during the initial stages of deformation.

4. Prediction of the ease of slip operation by SOF

4.1 Conditions for SOF calculation

The geometric model was subjected to tensile loading (Fig. 4b). The model was assumed to be the same as that for the current CPFEE analysis, and the spatial distributions of the ease of slip operation were evaluated by SOF. The slip systems similar to those used in the CPFEE analysis were assumed (Fig. 5). The parameters for the calculation of SOF are shown in Table 4. CRSSs were the same as those for the CPFEE analysis, and the values were determined in accordance with the experimental results by Pagan et al. (2017). The SOF spatial distributions were calculated with the changes in the influence range, as shown in Table 4 (I)–(V).

4.2 Distributions of SOF and comparison with CPFEE analysis results

Figs. 9a–e represent the SOF distributions under the conditions of Table 4. The distribution of slip strain obtained by the CPFEE analysis is shown in Fig. 9f. SOF defined by Eq. (8) represents the ease of slip operation considering the non-local interaction among the regions. The dependency of the influence ranges (r_e^{LD} and r_e^{TD}) on the distributions of SOF is as follows. When the influence ranges equal the average grain size ($r_e^{LD} = r_e^{TD} = D_{ave}$), the distribution of SOF (Fig. 9a) has a good correspondence with that of γ_{total} (Fig. 9f). When $r_e^{LD} = 2D_{ave}$ and $r_e^{TD} = D_{ave}$ (Fig. 9b), the difference between the values among the regions becomes more distinct. SOF in region “A” becomes low, and the distribution in the region becomes similar to that of γ_{total} , although the

1 distributions in Figs. 9a-b do not differ substantially. When $r_e^{LD} = D_{ave}$ and $r_e^{TD} = 2D_{ave}$
2 (Fig. 9c), SOF becomes higher in the regions closer to the grain boundary, and the
3 distribution does not correspond to that of γ_{total} . When $r_e^{LD} = r_e^{TD} = 2D_{ave}$ (Fig. 9d), the
4 distribution is similar to that in Fig. 9a. When $r_e^{LD} = 3D_{ave}$ and $r_e^{TD} = 2D_{ave}$ (Fig. 9e),
5 the high slip strain in region “B” cannot be predicted, whereas high SOF extended in the
6 Y-direction appears in region “C”, which captures the feature in the distribution of γ_{total}
7 in the grain.

8

9 The above results indicate: i) the strain distribution at the yielding point can be predicted
10 by SOF when appropriate r_e^{LD} and r_e^{TD} are employed; ii) r_e^{LD} , r_e^{TD} , and the ratio
11 between them strongly affect the prediction accuracy in the strain distribution; and iii)
12 appropriate r_e^{LD} and r_e^{TD} differ depending on the region as the prediction accuracy of
13 strain distribution in each region is different when r_e^{LD} and r_e^{TD} change. However, the
14 prediction accuracy of strain distribution by SOF decreases with the deformation. One of
15 the reasons for that is the activation of the secondary slip systems. However, the effect of
16 secondary slip systems is not taken into consideration in SOF.

17

18

19

20

21

22

1 **5. Discussion**

2
3 Here, we discuss why SOF could accurately predict the strain distributions and the
4 existence of the partial difference in the distributions obtained by the SOF and CPFE
5 analysis. Initially, we compare the distributions of SOF, SF, and NSF to investigate the
6 effect of interactions among the regions on the strain distributions. Then, we investigate
7 the effect of anisotropic elasticity and lattice rotation with plastic deformation on the
8 strain distribution to reveal the reasons for the difference.

9 10 **5.1 Comparison of SF and NSF distributions**

11
12 Herein, we compare the distributions of SOF with those of SF and NSF. Fig. 10 shows
13 the SF distributions. The distributions were evaluated using the maximum SF value
14 among all of the slip systems (Fig. 10a) and in individual slip systems (Fig. 10b). Fig. 11
15 shows the NSF distributions. The maximum values among the slip systems (m^{\max}) were
16 employed to reveal the distribution.

17
18 The SF distributions do not predict the strain distribution (Fig. 7a), and the NSF
19 distributions also do not show a good correspondence with the strain distribution in the
20 regions indicated by arrows in Fig. 11. The inhomogeneous distribution within each
21 crystal grain (Fig. 11) cannot be represented by SF and NSF, although NSF performs the
22 predictions more accurately than SF does by considering CRSSs. That is, SOF predicts
23 the strain distributions more accurately than SF and NSF do by considering the
24 interactions among the “soft” and “hard” regions, which can be distant or adjacent to each

1 other.

2

3 **5.2 Effect of anisotropic elasticity on strain distribution**

4

5 Anisotropic elasticity contributes to the inhomogeneous deformation in polycrystals at
6 the early stages of deformation (Hook and Hirth, 1967a; Kondou et al., 2008; Mayama et
7 al., 2009; Kawano et al., 2015; Tada and Uemori, 2018; Kawano et al., 2018a). In this
8 study, we investigate the effect of elastic anisotropy on the inhomogeneous deformation
9 in polycrystalline α -Ti. The results were obtained under the conditions of anisotropic or
10 isotropic elasticity and can be seen in Fig. 12. Other conditions were the same as those
11 mentioned in Figs. 7 and 8, except for the elasticity. The Poisson's ratio ($E = 106.3$ GPa)
12 and Young's modulus ($\nu = 0.34$) from polycrystalline CP-Ti were employed for the
13 isotropic elasticity. As for the isotropic elasticity condition, the elasticity was assumed to
14 be homogeneous for the whole geometric model.

15

16 The obtained macroscopic stress-strain relationship values were similar (Fig. 12c).
17 However, the distributions of the slip strain were different at the initial deformation stages
18 (Figs. 12a and b). When the slip deformation started to occur, the distribution within each
19 crystal was homogeneous on the condition of isotropic elasticity (Fig. 12a) with $\overline{\varepsilon_{XX}} =$
20 0.004. In contrast, the distribution within each crystal was inhomogeneous on the
21 condition of anisotropic elasticity due to the localized slip operation (Fig. 12b) with $\overline{\varepsilon_{XX}}$
22 = 0.004. The difference between the distributions immediately disappeared with the
23 deformation (Figs. 12a $\overline{\varepsilon_{XX}} = 0.005$ and 0.006). As a result, the effect of elastic

1 anisotropy on the distribution of slip strain is negligible near the yielding point of the
2 current analysis.

3 4 **5.3 Effect of lattice rotation on strain distribution**

5
6 Herein, we investigate the effect of lattice rotation with the deformation on the
7 inhomogeneous deformation. Figs. 13a–d show the pole figures, and Figs. 13e–f represent
8 the changes in the angles of vectors normal to (0001) and $\{10\bar{1}0\}$ planes from the initial
9 states when $\overline{\varepsilon_{XX}} = 0.031$.

10
11 The changes in the pole figures were negligible even when $\overline{\varepsilon_{XX}} = 0.031$ (Figs. 13a-d). The
12 changes in the angles of vectors normal to the planes were insignificant, and the average
13 angle change was $< 2^\circ$, although the localized, substantial changes in the angles existed.

14 The changes near the yielding point ($\overline{\varepsilon_{XX}} \approx 0.006$) were much smaller than those at $\overline{\varepsilon_{XX}}$
15 $= 0.031$. Consequently, although the lattice rotation is an important factor for the
16 understanding of deformation mechanisms, its effect on the inhomogeneous deformation
17 is negligible near the yielding point in the current analysis.

18 19 **5.4 Other effects and future studies**

20
21 A number of effects might cause the difference in the distributions of ε_{XX} , as predicted
22 by CPFEE and SOF. In this study, the following effects were discussed: the activation of
23 the secondary slip systems, anisotropic elasticity, and lattice rotation. SOF predicted the

1 strain distribution accurately near the yielding point; nevertheless, the effects of the
2 secondary slip systems and lattice rotation tend to increase with deformation, and it is
3 difficult to predict the strain distributions in the larger deformation stage by the current
4 SOF. Other effects, such as deformation incompatibility between the crystal grains, also
5 may contribute to the inhomogeneous deformation (Hook and Hirth, 1967b; Kondou et
6 al., 2008; Kawano et al., 2015; Kawano et al., 2018a).

7
8 As stated above, SOF can predict the distributions of normal strain along the tensile
9 direction obtained by the crystal plasticity analysis. The crystal plasticity analysis is a
10 method that allows to reproduce the distributions of strain obtained by the experiments
11 (Raabe et al., 2001; Zhao et al., 2008; Weinberger et al., 2014; Tasan et al., 2014; Guery
12 et al., 2016b; Zhang et al., 2018b; Kawano et al., 2019b). Therefore, it is possible that
13 SOF can reproduce the strain distributions obtained by the experiments (e.g., DIC). In
14 addition, SOF was evaluated using the influence ranges (r_e^{LD} and r_e^{TD}), i.e., the
15 interaction ranges among the regions can be investigated by SOF. The calculation cost of
16 SOF is much lower than that of FEM. Thus, it is an effective indicator that can be used
17 for the understanding of the deformation mechanisms in the microstructures of crystalline
18 materials. Furthermore, it is possible that the effects of size (Okazaki and Conrad, 1972;
19 Sergueeva et al., 2001) and the second phase (Radecka et al., 2016) will be taken into
20 account in SOF by the change in CRSSs, depending on their effects. When SOF
21 considering these effects is developed, the strain distributions in materials with the second
22 phase and finer grains will be predicted. SOF can be used in future studies to reveal the
23 deformation mechanisms at the crystal grain level.

6. Conclusions

In this study, we developed an indicator, namely, a slip operation factor (SOF), to represent the ease of slip operation at a lower computational cost. We also considered the relative plastic deformability among the regions, which is a function of the Schmid factor and CRSS. SOF was adapted to a microstructural map of polycrystalline α -Ti, obtained by EBSD, and several distributions of SOF were acquired by changing the influence ranges (r_e^{LD} and r_e^{TD}) under the condition of uniaxial tension. The obtained distributions were compared with those of the strains predicted by the crystal plasticity finite element (CPFE) analysis. The results can be summarized as follows:

- (1) SOF can predict the spatial distributions of slip strain more accurately than the Schmid factor (SF) or normalized Schmid factor (NSF) when the appropriate influence ranges (r_e^{LD} and r_e^{TD}) are employed.
- (2) In its current form, SOF can predict the normal strain in the tensile direction near the yielding point. This is because the effects of anisotropic elasticity, activation of the secondary slip systems, lattice rotation, and deformation incompatibility have negligible impacts on the inhomogeneous deformation near the yielding point, whereas the relative deformability among the plastically “soft” and “hard” regions strongly affects the strain distributions.
- (3) The difference in the distributions of SOF and normal strains in the tensile

1 direction increases with the deformation after the yielding point due to the
2 activation of secondary slip systems. However, the impacts of anisotropic
3 elasticity and lattice rotation were minor on the inhomogeneous deformation when
4 $\varepsilon \approx 0.03$.

5
6 (4) The prediction accuracy of strain distributions differs depending on the regions
7 and changes with r_e^{LD} and r_e^{TD} . Therefore, the mechanical interaction range may
8 vary depending on the region.

9
10 (5) The mechanical interactions among the adjacent crystal grains in inhomogeneous
11 deformation in α -Ti have been studied, while little attention has been paid to
12 longer-range interactions. The current analysis using SOF showed the importance
13 of the longer-range interaction for the inhomogeneous deformation as well as the
14 interactions among the adjacent grains.

1 **Appendix: Constitutive model for CPFEE analysis**

2

3 The rate-dependent finite strain crystal plasticity model proposed by Peirce et al. (1983)
4 was employed in this study. The velocity gradient L was calculated as

5

6
$$\mathbf{L} = \mathbf{L}^* + \mathbf{L}^p, \tag{A1}$$

7

8 where L^* and L^p are the elastic and plastic velocity gradients, respectively. The
9 deformation rate tensor D and spin tensor W were calculated as follows:

10

11
$$\mathbf{D} = \frac{\mathbf{L} + \mathbf{L}^T}{2}, \tag{A2}$$

12
$$\mathbf{W} = \frac{\mathbf{L} - \mathbf{L}^T}{2}, \tag{A3}$$

13

14 where L^T is the transposed matrix of L .

15

16 The slip contribution of slip system α to the plastic velocity gradient was defined as

17

18
$$\mathbf{L}^{p(k)} = \dot{\gamma}^{(k)} \left(\mathbf{s}^{(k)} \otimes \mathbf{m}^{(k)} \right), \tag{A4}$$

19

20 and the plastic velocity gradient was calculated as the sum of the contributions of all the
21 slip systems

22

$$1 \quad \mathbf{L}^P = \sum_{k=1}^N \dot{\gamma}^{(k)} \left(\mathbf{s}^{(k)} \otimes \mathbf{m}^{(k)} \right), \quad (\text{A5})$$

2

3 where N is the number of slip systems. The plastic deformation rate tensor and the
4 plastic spin tensor were defined as

5

$$6 \quad \mathbf{D}^P = \frac{\mathbf{L}^P + \mathbf{L}^{P^T}}{2} = \sum_{\alpha=1}^N \dot{\gamma}^{(\alpha)} \left[\frac{\mathbf{s}^{(\alpha)} \otimes \mathbf{m}^{(\alpha)} + \mathbf{m}^{(\alpha)} \otimes \mathbf{s}^{(\alpha)}}{2} \right] \equiv \sum_{\alpha=1}^N \dot{\gamma}^{(\alpha)} \mathbf{p}^{(\alpha)}, \quad (\text{A6})$$

$$7 \quad \mathbf{W}^P = \frac{\mathbf{L}^P - \mathbf{L}^{P^T}}{2} = \sum_{\alpha=1}^N \dot{\gamma}^{(\alpha)} \left[\frac{\mathbf{s}^{(\alpha)} \otimes \mathbf{m}^{(\alpha)} - \mathbf{m}^{(\alpha)} \otimes \mathbf{s}^{(\alpha)}}{2} \right] \equiv \sum_{\alpha=1}^N \dot{\gamma}^{(\alpha)} \mathbf{w}^{(\alpha)}. \quad (\text{A7})$$

8

9 The elastic deformation rate tensor \mathbf{D}^* and elastic spin tensor \mathbf{W}^* were calculated as

10

$$11 \quad \mathbf{D}^* = \frac{\mathbf{L}^* + \mathbf{L}^{*T}}{2}, \quad (\text{A8})$$

$$12 \quad \mathbf{W}^* = \frac{\mathbf{L}^* - \mathbf{L}^{*T}}{2}. \quad (\text{A9})$$

13

14 The following elastic constitutive equation was employed:

15

$$16 \quad \overset{\nabla}{\boldsymbol{\sigma}}^* = \dot{\boldsymbol{\sigma}} - \mathbf{W}^* \boldsymbol{\sigma} + \boldsymbol{\sigma} \mathbf{W}^* = \mathbf{C} : \mathbf{D}^*, \quad (\text{A10})$$

17

18 where \mathbf{C} is the fourth-order elastic stiffness tensor.

19 The elastoplastic deformation tensor was assumed to be

1

$$\mathbf{D} = \mathbf{D}^* + \mathbf{D}^p . \quad (\text{A11})$$

3

4 The relationship between the elastic stress rate and \mathbf{D} was given by

5

$$\overset{\nabla}{\boldsymbol{\sigma}}^* = \mathbf{C} : \mathbf{D} - \sum_{\alpha=1}^N \dot{\gamma}^{(\alpha)} \mathbf{C} : \mathbf{p}^{(\alpha)} . \quad (\text{A12})$$

7

8 The Jourmann stress rate was calculated as

9

$$\overset{\nabla}{\boldsymbol{\sigma}} = \dot{\boldsymbol{\sigma}} - \mathbf{W} \boldsymbol{\sigma} + \mathbf{W} \boldsymbol{\sigma} , \quad (\text{A13})$$

11

12 and the following relationship was obtained from Eqs. (A7), (A10), (A12), and elastic

13 and plastic decomposition of spin tensor \mathbf{W} as

14

$$\overset{\nabla}{\boldsymbol{\sigma}} = \mathbf{C} : \mathbf{D} - \sum_{\alpha=1}^N \dot{\gamma}^{(\alpha)} \left[\mathbf{C} : \mathbf{p}^{(\alpha)} + \mathbf{w}^{(\alpha)} \boldsymbol{\sigma} - \boldsymbol{\sigma} \mathbf{w}^{(\alpha)} \right] . \quad (\text{A14})$$

16

17 Changes in the directions of \mathbf{s} and \mathbf{m} according to the rotation of crystal lattice were

18 determined as

19

$$\dot{\mathbf{m}}^{(\alpha)} = \mathbf{W}^* \mathbf{m}^{(\alpha)} , \quad (\text{A15})$$

$$\dot{\mathbf{s}}^{(\alpha)} = \mathbf{W}^* \mathbf{s}^{(\alpha)} . \quad (\text{A16})$$

22

1

2

3 **Acknowledgments**

4

5 The authors are grateful to professors T. Ohashi and J. Shibano from the Kitami Institute
6 of Technology (KIT) for the organization of an efficient research environment. M.
7 Hasegawa is thanked for setting up the computers for the numerical simulations. This
8 work was partially supported by the JSPS KAKENHI (number JP19K04983) and Amada
9 Foundation grants (number AF-2018036-C2).

1 **References**

2

- 3 Abdolvand, H., Wright, J., Wilkinson, A.J., 2018. Strong grain neighbour effects in
4 polycrystals. *Nat. Commun.* 9, 1–11. <https://doi.org/10.1038/s41467-017-02213-9>
- 5 Aoyagi, Y., Tsuru, T., Shimokawa, T., 2014. Crystal plasticity modeling and simulation
6 considering the behavior of the dislocation source of ultrafine-grained metal. *Int. J.*
7 *Plast.* 55, 43–57. <https://doi.org/10.1016/j.ijplas.2013.09.009>
- 8 Ardeljan, M., Beyerlein, I.J., McWilliams, B.A., Knezevic, M., 2016. Strain rate and
9 temperature sensitive multi-level crystal plasticity model for large plastic
10 deformation behavior: Application to AZ31 magnesium alloy. *Int. J. Plast.* 83, 90–
11 109. <https://doi.org/10.1016/j.ijplas.2016.04.005>
- 12 Asaro, R.J., Needleman, A., 1985. Texture development and strain hardening in rate
13 dependent polycrystals. *Acta Metall.* 33, 923–953. [https://doi.org/10.1016/0001-](https://doi.org/10.1016/0001-6160(85)90188-9)
14 6160(85)90188-9
- 15 Asaro, R.J., Rice, J.R., 1977. Strain localization in ductile single crystals. *J. Mech.*
16 *Phys. Solids* 25, 309–338. [https://doi.org/10.1016/0022-5096\(77\)90001-1](https://doi.org/10.1016/0022-5096(77)90001-1)
- 17 Asim, U.B., Siddiq, M.A., Kartal, M.E., 2019. Representative volume element (RVE)
18 based crystal plasticity study of void growth on phase boundary in titanium alloys.
19 *Comput. Mater. Sci.* 161, 346–350.
20 <https://doi.org/10.1016/j.commatsci.2019.02.005>
- 21 Bache, M.R., 2003. A review of dwell sensitive fatigue in titanium alloys: the role of
22 microstructure, texture and operating conditions. *Int. J. Fatigue* 25, 1079–1087.
23 [https://doi.org/10.1016/S0142-1123\(03\)00145-2](https://doi.org/10.1016/S0142-1123(03)00145-2)
- 24 Bantounas, I., Dye, D., Lindley, T.C., 2009. The effect of grain orientation on fracture

1 morphology during high-cycle fatigue of Ti–6Al–4V. *Acta Mater.* 57, 3584–3595.
2 <https://doi.org/10.1016/j.actamat.2009.04.018>

3 Bao, L., Schuman, C., Lecomte, J.S., Philippe, M.J., Zhao, X., Esling, C., 2011. A study
4 of twin variant selection and twin growth in titanium. *Adv. Eng. Mater.* 13, 928–
5 932. <https://doi.org/10.1002/adem.201100055>

6 Barlat, F., Gracio, J.J., Lee, M.-G., Rauch, E.F., Vincze, G., 2011. An alternative to
7 kinematic hardening in classical plasticity. *Int. J. Plast.* 27, 1309–1327.
8 <https://doi.org/10.1016/j.ijplas.2011.03.003>

9 Benmhenni, N., Bouvier, S., Brenner, R., Chauveau, T., Bacroix, B., 2013.
10 Micromechanical modelling of monotonic loading of CP α -Ti: Correlation between
11 macroscopic and microscopic behaviour. *Mater. Sci. Eng. A* 573, 222–233.
12 <https://doi.org/10.1016/j.msea.2013.02.022>

13 Berdichevsky, V.L., 2006. Continuum theory of dislocations revisited. *Contin. Mech.*
14 *Thermodyn.* 18, 195–222. <https://doi.org/10.1007/s00161-006-0024-7>

15 Beyerlein, I.J., Tomé, C.N., 2008. A dislocation-based constitutive law for pure Zr
16 including temperature effects. *Int. J. Plast.* 24, 867–895.
17 <https://doi.org/10.1016/j.ijplas.2007.07.017>

18 Bieler, T.R., Eisenlohr, P., Zhang, C., Phukan, H.J., Crimp, M.A., 2014. Grain
19 boundaries and interfaces in slip transfer. *Curr. Opin. Solid State Mater. Sci.* 18,
20 212–226. <https://doi.org/10.1016/j.cossms.2014.05.003>

21 Bridier, F., Villechaise, P., Mendez, J., 2005. Analysis of the different slip systems
22 activated by tension in a α/β titanium alloy in relation with local crystallographic
23 orientation. *Acta Mater.* 53, 555–567.
24 <https://doi.org/10.1016/j.actamat.2004.09.040>

- 1 Capolungo, L., Marshall, P.E., McCabe, R.J., Beyerlein, I.J., Tomé, C.N., 2009.
2 Nucleation and growth of twins in Zr: A statistical study. *Acta Mater.* 57, 6047–
3 6056. <https://doi.org/10.1016/j.actamat.2009.08.030>
- 4 Cereceda, D., Diehl, M., Roters, F., Raabe, D., Perlado, J.M., Marian, J., 2016.
5 Unraveling the temperature dependence of the yield strength in single-crystal
6 tungsten using atomistically-informed crystal plasticity calculations. *Int. J. Plast.*
7 78, 242–265. <https://doi.org/10.1016/j.ijplas.2015.09.002>
- 8 Conrad, H., 1981. Effect of interstitial solutes on the strength and ductility of titanium.
9 *Prog. Mater. Sci.* 26, 123–403. [https://doi.org/10.1016/0079-6425\(81\)90001-3](https://doi.org/10.1016/0079-6425(81)90001-3)
- 10 Dunne, F.P.E., Rugg, D., 2008. On the mechanisms of fatigue facet nucleation in
11 titanium alloys. *Fatigue Fract. Eng. Mater. Struct.* 31, 949–958.
12 <https://doi.org/10.1111/j.1460-2695.2008.01284.x>
- 13 Dunne, F.P.E., Rugg, D., Walker, A., 2007a. Lengthscale-dependent, elastically
14 anisotropic, physically-based hcp crystal plasticity: Application to cold-dwell
15 fatigue in Ti alloys. *Int. J. Plast.* 23, 1061–1083.
16 <https://doi.org/10.1016/j.ijplas.2006.10.013>
- 17 Dunne, F.P.E., Walker, A., Rugg, D., 2007b. A systematic study of hcp crystal
18 orientation and morphology effects in polycrystal deformation and fatigue. *Proc. R.*
19 *Soc. A Math. Phys. Eng. Sci.* 463, 1467–1489.
20 <https://doi.org/10.1098/rspa.2007.1833>
- 21 El Kadiri, H., Baird, J.C., Kapil, J., Oppedal, A.L., Cherkaoui, M., Vogel, S.C., 2013.
22 Flow asymmetry and nucleation stresses of {1012} twinning and non-basal slip in
23 magnesium. *Int. J. Plast.* 44, 111–120. <https://doi.org/10.1016/j.ijplas.2012.11.004>
- 24 Evans, W.J., 1998. Optimising mechanical properties in alpha+beta titanium alloys.

1 Mater. Sci. Eng. A 243, 89–96. [https://doi.org/10.1016/S0921-5093\(97\)00784-3](https://doi.org/10.1016/S0921-5093(97)00784-3)

2 Fisher, E.S., Renken, C.J., 1964. Single-crystal elastic moduli and the hcp → bcc
3 transformation in Ti, Zr, and Hf. Phys. Rev. 135, A482–A494.
4 <https://doi.org/10.1103/PhysRev.135.A482>

5 Fitzner, A., Prakash, D.G.L., da Fonseca, J.Q., Thomas, M., Zhang, S.-Y., Kelleher, J.,
6 Manuel, P., Preuss, M., 2016. The effect of aluminium on twinning in binary
7 alpha-titanium. Acta Mater. 103, 341–351.
8 <https://doi.org/10.1016/j.actamat.2015.09.048>

9 Guery, A., Hild, F., Latourte, F., Roux, S., 2016a. Identification of crystal plasticity
10 parameters using DIC measurements and weighted FEMU. Mech. Mater. 100, 55–
11 71. <https://doi.org/10.1016/j.mechmat.2016.06.007>

12 Guery, A., Hild, F., Latourte, F., Roux, S., 2016b. Slip activities in polycrystals
13 determined by coupling DIC measurements with crystal plasticity calculations. Int.
14 J. Plast. 81, 249–266. <https://doi.org/10.1016/j.ijplas.2016.01.008>

15 Hama, T., Kobuki, A., Takuda, H., 2017. Crystal-plasticity finite-element analysis of
16 anisotropic deformation behavior in a commercially pure titanium Grade 1 sheet.
17 Int. J. Plast. 91, 77–108. <https://doi.org/10.1016/j.ijplas.2016.12.005>

18 Hanada, S., 1990. Plastic Deformation Mechanisms in α Titanium. Tetsu-to-Hagane (in
19 Japanese) 76, 495–502. https://doi.org/10.2355/tetsutohagane1955.76.4_495

20 Hasija, V., Ghosh, S., Mills, M.J., Joseph, D.S., 2003. Deformation and creep modeling
21 in polycrystalline Ti-6Al alloys. Acta Mater. 51, 4533–4549.
22 [https://doi.org/10.1016/S1359-6454\(03\)00289-1](https://doi.org/10.1016/S1359-6454(03)00289-1)

23 Hook, R.E., Hirth, J.P., 1967a. The deformation behavior of isoaxial bicrystals of Fe-
24 3%Si. Acta Metall. 15, 535–551. [https://doi.org/10.1016/0001-6160\(67\)90087-9](https://doi.org/10.1016/0001-6160(67)90087-9)

1 Hook, R.E., Hirth, J.P., 1967b. The deformation behavior of non-isoaxial bicrystals of
2 Fe-3% Si. *Acta Metall.* 15, 1099–1110. <https://doi.org/10.1016/0001->
3 [6160\(67\)90383-5](https://doi.org/10.1016/0001-6160(67)90383-5)

4 Kawano, Y., Ohashi, T., Mayama, T., Kondou, R., 2018a. Crystal plasticity analysis of
5 change in incompatibility and activities of slip systems in α -phase of Ti alloy under
6 cyclic loading. *Int. J. Mech. Sci.* 146–147, 475–485.
7 <https://doi.org/10.1016/j.ijmecsci.2017.09.023>

8 Kawano, Y., Ohashi, T., Mayama, T., Mitsuhashi, M., Okuyama, Y., Sato, M., 2019a.
9 Crystal Plasticity Analysis of Microscopic Deformation Mechanisms and GN
10 Dislocation Accumulation Depending on Vanadium Content in β Phase of Two-
11 Phase Ti Alloy. *Mater. Trans.* 60, 959–968.
12 <https://doi.org/doi:10.2320/matertrans.M2019016>

13 Kawano, Y., Ohashi, T., Mayama, T., Tanaka, M., Okuyama, Y., Sato, M., 2019b.
14 Investigation of strain redistribution mechanism in α titanium by image-based
15 crystal plasticity analysis. *Eur. Phys. J. B* 92, 204.
16 <https://doi.org/10.1140/epjb/e2019-100238-3>

17 Kawano, Y., Ohashi, T., Mayama, T., Tanaka, M., Sakamoto, M., Okuyama, Y., Sato,
18 M., 2018b. Development of a EBSD-FEM data conversion interface and the
19 image-based crystal plasticity analysis. *Trans. JSME (in Japanese)* 84, 17-00559:1–
20 18. <https://doi.org/10.1299/transjsme.17-00559>

21 Kawano, Y., Tamaru, N., Ishii, S., Mayama, T., Kondou, R., Ohashi, T., 2015. Grain
22 boundary inclination dependence of GN dislocation patterns and density in
23 bicrystal model. *Trans. JSME (in Japanese)* 81, 14-00630:1–14.
24 <https://doi.org/10.1299/transjsme.14-00630>

- 1 Knezevic, M., Beyerlein, I.J., Brown, D.W., Sisneros, T.A., Tomé, C.N., 2013. A
2 polycrystal plasticity model for predicting mechanical response and texture
3 evolution during strain-path changes : Application to beryllium. *Int. J. Plast.* 49,
4 185–198. <https://doi.org/10.1016/j.ijplas.2013.03.008>
- 5 Kocks, U.F., 1976. Laws for Work-Hardening and Low-Temperature Creep. *J. Eng.*
6 *Mater. Technol.* 98, 76–85. <https://doi.org/10.1115/1.3443340>
- 7 Kondou, R., Ohashi, T., Miura, S., 2008. Relationship between micro-incompatibility
8 and heterogeneity of dislocation density distribution in Cu-9at.% Al symmetric
9 type bicrystal models under tensile Loading. *J. Comput. Sci. Technol.* 2, 162–172.
10 <https://doi.org/10.1299/jcst.2.162>
- 11 Koster, M., Le, K.C., Nguyen, B.D., 2015. Formation of grain boundaries in ductile
12 single crystals at finite plastic deformations. *Int. J. Plast.* 69, 134–151.
13 <https://doi.org/10.1016/j.ijplas.2015.02.010>
- 14 Kotha, S., Ozturk, D., Ghosh, S., 2019. Parametrically homogenized constitutive
15 models (PHCMs) from micromechanical crystal plasticity FE simulations, part I:
16 Sensitivity analysis and parameter identification for Titanium alloys. *Int. J. Plast.*
17 120, 296–319. <https://doi.org/10.1016/j.ijplas.2019.05.008>
- 18 Kuroda, M., Tvergaard, V., 2006. Studies of scale dependent crystal viscoplasticity
19 models. *J. Mech. Phys. Solids* 54, 1789–1810.
20 <https://doi.org/10.1016/j.jmps.2006.04.002>
- 21 Langer, J.S., 2016. Thermal effects in dislocation theory. *Phys. Rev. E* 94, 063004:1–9.
22 <https://doi.org/10.1103/PhysRevE.94.063004>
- 23 Langer, J.S., 2015. Statistical thermodynamics of strain hardening in polycrystalline
24 solids. *Phys. Rev. E* 92, 032125:1–9. <https://doi.org/10.1103/PhysRevE.92.032125>

- 1 Langer, J.S., Bouchbinder, E., Lookman, T., 2010. Thermodynamic theory of
2 dislocation-mediated plasticity. *Acta Mater.* 58, 3718–3732.
3 <https://doi.org/10.1016/j.actamat.2010.03.009>
- 4 Le, K.C., 2018. Thermodynamic dislocation theory for non-uniform plastic
5 deformations. *J. Mech. Phys. Solids* 111, 157–169.
6 <https://doi.org/10.1016/j.jmps.2017.10.022>
- 7 Le, K.C., Günther, C., 2014. Nonlinear continuum dislocation theory revisited. *Int. J.*
8 *Plast.* 53, 164–178. <https://doi.org/10.1016/j.ijplas.2013.08.003>
- 9 Le, K.C., Nguyen, B.D., 2013. On bending of single crystal beam with continuously
10 distributed dislocations. *Int. J. Plast.* 48, 152–167.
11 <https://doi.org/10.1016/j.ijplas.2013.02.010>
- 12 Le, K.C., Nguyen, B.D., 2012. Polygonization: Theory and comparison with
13 experiments. *Int. J. Eng. Sci.* 59, 211–218.
14 <https://doi.org/10.1016/j.ijengsci.2012.03.005>
- 15 Le, K.C., Sembiring, P., 2008. Analytical solution of plane constrained shear problem
16 for single crystals within continuum dislocation theory. *Arch. Appl. Mech.* 78,
17 587–597. <https://doi.org/10.1007/s00419-007-0178-1>
- 18 Le, K.C., Stumpf, H., 1996. A model of elastoplastic bodies with continuously
19 distributed dislocations. *Int. J. Plast.* 12, 611–627. [https://doi.org/10.1016/S0749-](https://doi.org/10.1016/S0749-6419(96)00022-8)
20 [6419\(96\)00022-8](https://doi.org/10.1016/S0749-6419(96)00022-8)
- 21 Le, K.C., Tran, T.M., Langer, J.S., 2017. Thermodynamic dislocation theory of high-
22 temperature deformation in aluminum and steel. *Phys. Rev. E* 96, 013004:1–7.
23 <https://doi.org/10.1103/PhysRevE.96.013004>
- 24 Lee, M.G., Lim, H., Adams, B.L., Hirth, J.P., Wagoner, R.H., 2010. A dislocation

1 density-based single crystal constitutive equation. *Int. J. Plast.* 26, 925–938.
2 <https://doi.org/10.1016/j.ijplas.2009.11.004>

3 Lewandowski, M.J., Stupkiewicz, S., 2018. Size effects in wedge indentation predicted
4 by a gradient-enhanced crystal-plasticity model. *Int. J. Plast.* 109, 54–78.
5 <https://doi.org/10.1016/j.ijplas.2018.05.008>

6 Lütjering, G., Williams, J.C., 2007. *Titanium, 2nd Edition (Engineering and Processes),*
7 *Engineering Materials, Processes.* Springer Berlin Heidelberg, Berlin, Heidelberg.
8 <https://doi.org/10.1007/978-3-540-73036-1>

9 Mayama, T., Noda, M., Chiba, R., Kuroda, M., 2011. Crystal plasticity analysis of
10 texture development in magnesium alloy during extrusion. *Int. J. Plast.* 27, 1916–
11 1935. <https://doi.org/10.1016/j.ijplas.2011.02.007>

12 Mayama, T., Ohashi, T., Kondou, R., 2009. Geometrically necessary dislocation
13 structure organization in FCC bicrystal subjected to cyclic plasticity. *Int. J. Plast.*
14 25, 2122–2140. <https://doi.org/10.1016/j.ijplas.2009.02.001>

15 Monaghan, J.J., 1988. An introduction to SPH. *Comput. Phys. Commun.* 48, 89–96.
16 [https://doi.org/10.1016/0010-4655\(88\)90026-4](https://doi.org/10.1016/0010-4655(88)90026-4)

17 Müller, M., Charypar, D., Gross, M., 2003. Particle-based fluid simulation for
18 interactive applications. *Proc. 2003 ACM SIGGRAPH/Eurographics Symp.*
19 *Comput. Animat.* 154–159.
20 <https://doi.org/http://portal.acm.org/citation.cfm?id=846298>

21 Ohashi, T., 2018. Generation and accumulation of atomic vacancies due to dislocation
22 movement and pair annihilation. *Philos. Mag.* 98, 2275–2295.
23 <https://doi.org/10.1080/14786435.2018.1478142>

24 Ohashi, T., 1997. Finite-element analysis of plastic slip and evolution of geometrically

1 necessary dislocations in fcc crystals. *Philos. Mag. Lett.* 75, 51–58.
2 <https://doi.org/10.1080/095008397179741>

3 Ohashi, T., 1994. Numerical modelling of plastic multislip in metal crystals of F.C.C.
4 type. *Philos. Mag. A Phys. Condens. Matter, Struct. Defects Mech. Prop.* 70, 793–
5 803. <https://doi.org/10.1080/01418619408242931>

6 Ohashi, T., Kawamukai, M., Zbib, H., 2007. A multiscale approach for modeling scale-
7 dependent yield stress in polycrystalline metals. *Int. J. Plast.* 23, 897–914.
8 <https://doi.org/10.1016/j.ijplas.2006.10.002>

9 Ohashi, T., Okuyama, Y., 2019. Density evolution of atomic vacancies in copper single
10 crystals during initial stage of fatigue deformation. *Philos. Mag.*
11 <https://doi.org/10.1080/14786435.2019.1659517>

12 Okazaki, K., Conrad, H., 1972. Thermal and athermal components of the flow stress in
13 zone-refined titanium. *Trans. Japan Inst. Met.* 13, 205–213.
14 <https://doi.org/10.2320/matertrans1960.13.205>

15 Pagan, D.C., Shade, P.A., Barton, N.R., Park, J.-S., Kenesei, P., Menasche, D.B.,
16 Bernier, J. V., 2017. Modeling slip system strength evolution in Ti-7Al informed
17 by in-situ grain stress measurements. *Acta Mater.* 128, 406–417.
18 <https://doi.org/10.1016/j.actamat.2017.02.042>

19 Peirce, D., Asaro, R.J., Needleman, A., 1983. Material rate dependence and localized
20 deformation in crystalline solids. *Acta Metall.* 31, 1951–1976.
21 [https://doi.org/10.1016/0001-6160\(83\)90014-7](https://doi.org/10.1016/0001-6160(83)90014-7)

22 Peirce, D., Asaro, R.J., Needleman, A., 1982. An analysis of nonuniform and localized
23 deformation in ductile single crystals. *Acta Metall.* 30, 1087–1119.
24 [https://doi.org/10.1016/0001-6160\(82\)90005-0](https://doi.org/10.1016/0001-6160(82)90005-0)

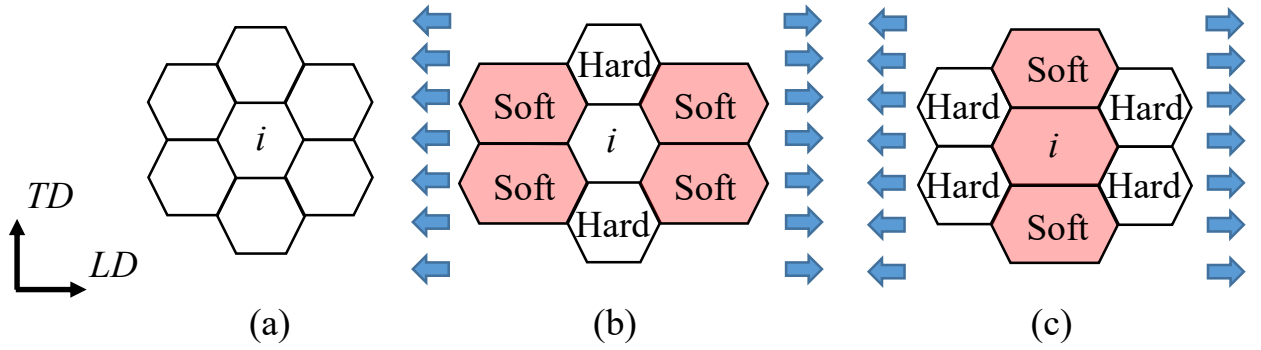
- 1 Philippe, M.J., Serghat, M., Vanhoutte, P., Esling, C., 1995. Modeling of texture
2 evolution for materials of hexagonal symmetry -II. application to zirconium and
3 titanium α or near α alloys. *Acta Metall.* 43, 1619–1630.
4 [https://doi.org/10.1016/0956-7151\(94\)00329-g](https://doi.org/10.1016/0956-7151(94)00329-g)
- 5 Raabe, D., Sachtleber, M., Zhao, Z., Roters, F., Zaefferer, S., 2001. Micromechanical
6 and macromechanical effects in grain scale polycrystal plasticity experimentation
7 and simulation. *Acta Mater.* 49, 3433–3441. [https://doi.org/10.1016/S1359-](https://doi.org/10.1016/S1359-6454(01)00242-7)
8 [6454\(01\)00242-7](https://doi.org/10.1016/S1359-6454(01)00242-7)
- 9 Radecka, A., Bagot, P.A.J., Martin, T.L., Coakley, J., Vorontsov, V.A., Moody, M.P.,
10 Ishii, H., Rugg, D., Dye, D., 2016. The formation of ordered clusters in Ti-7Al and
11 Ti-6Al-4V. *Acta Mater.* 112, 141–149.
12 <https://doi.org/10.1016/j.actamat.2016.03.080>
- 13 Roters, F., Diehl, M., Shanthraj, P., Eisenlohr, P., Reuber, C., Wong, S.L., Maiti, T.,
14 Ebrahimi, A., Hochrainer, T., Fabritius, H.-O., Nikolov, S., Friák, M., Fujita, N.,
15 Grilli, N., Janssens, K.G.F., Jia, N., Kok, P.J.J., Ma, D., Meier, F., Werner, E.,
16 Stricker, M., Weygand, D., Raabe, D., 2019. DAMASK – The Düsseldorf
17 Advanced Material Simulation Kit for modeling multi-physics crystal plasticity,
18 thermal, and damage phenomena from the single crystal up to the component scale.
19 *Comput. Mater. Sci.* 158, 420–478.
20 <https://doi.org/10.1016/j.commatsci.2018.04.030>
- 21 Sergueeva, A., Stolyarov, V., Valiev, R., Mukherjee, A., 2001. Advanced mechanical
22 properties of pure titanium with ultrafine grained structure. *Scr. Mater.* 45, 747–
23 752. [https://doi.org/10.1016/S1359-6462\(01\)01089-2](https://doi.org/10.1016/S1359-6462(01)01089-2)
- 24 Sun, F., Meade, E.D., O’Dowd, N.P., 2019. Strain gradient crystal plasticity modelling

1 of size effects in a hierarchical martensitic steel using the Voronoi tessellation
2 method. *Int. J. Plast.* 119, 215–229. <https://doi.org/10.1016/j.ijplas.2019.03.009>
3 Sun, J., Jin, L., Dong, J., Wang, F., Dong, S., Ding, W., Luo, A.A., In press. Towards
4 high ductility in magnesium alloys - The role of intergranular deformation. *Int. J.*
5 *Plast.* 1–12. <https://doi.org/10.1016/j.ijplas.2019.07.014>
6 Tada, N., Uemori, T., 2018. Microscopic elastic and plastic inhomogeneous
7 deformations and height changes on the surface of a polycrystalline pure-titanium
8 plate specimen under cyclic tension. *Appl. Sci.* 8, 1907:1–10.
9 <https://doi.org/10.3390/app8101907>
10 Tasan, C.C., Diehl, M., Yan, D., Zambaldi, C., Shanthraj, P., Roters, F., Raabe, D.,
11 2014. Integrated experimental-simulation analysis of stress and strain partitioning
12 in multiphase alloys. *Acta Mater.* 81, 386–400.
13 <https://doi.org/10.1016/j.actamat.2014.07.071>
14 Tsuru, T., Shibutani, Y., Hirouchi, T., 2016. A predictive model for transferability of
15 plastic deformation through grain boundaries. *AIP Adv.* 6, 015004:1–9.
16 <https://doi.org/10.1063/1.4939819>
17 Voce, E., 1955. A practical strain-hardening function. *Metallurgia* 51, 219–226.
18 Waheed, S., Zheng, Z., Balint, D.S., Dunne, F.P.E., 2019. Microstructural effects on
19 strain rate and dwell sensitivity in dual-phase titanium alloys. *Acta Mater.* 162,
20 136–148. <https://doi.org/10.1016/J.ACTAMAT.2018.09.035>
21 Wang, L., Zheng, Z., Phukan, H., Kenesei, P., Park, J.S., Lind, J., Suter, R.M., Bieler,
22 T.R., 2017. Direct measurement of critical resolved shear stress of prismatic and
23 basal slip in polycrystalline Ti using high energy X-ray diffraction microscopy.
24 *Acta Mater.* 132, 598–610. <https://doi.org/10.1016/j.actamat.2017.05.015>

- 1 Warwick, J.L.W., Coakley, J., Raghunathan, S.L., Talling, R.J., Dye, D., 2012. Effect of
2 texture on load partitioning in Ti-6Al-4V. *Acta Mater.* 60, 4117–4127.
3 <https://doi.org/10.1016/j.actamat.2012.03.039>
- 4 Weinberger, C.R., Battaile, C.C., Lim, H., Carroll, J.D., Boyce, B.L., Buchheit, T.E.,
5 2014. Grain-scale experimental validation of crystal plasticity finite element
6 simulations of tantalum oligocrystals. *Int. J. Plast.* 60, 1–18.
7 <https://doi.org/10.1016/j.ijplas.2014.05.004>
- 8 Wu, X., Kalidindi, S.R., Necker, C., Salem, A.A., 2007. Prediction of crystallographic
9 texture evolution and anisotropic stress-strain curves during large plastic strains in
10 high purity α -titanium using a Taylor-type crystal plasticity model. *Acta Mater.* 55,
11 423–432. <https://doi.org/10.1016/j.actamat.2006.08.034>
- 12 Yoshida, F., Uemori, T., 2002. A model of large-strain cyclic plasticity describing the
13 Bauschinger effect and workhardening stagnation. *Int. J. Plast.* 18, 661–686.
14 [https://doi.org/10.1016/S0749-6419\(01\)00050-X](https://doi.org/10.1016/S0749-6419(01)00050-X)
- 15 Zhang, C., Li, H., Eisenlohr, P., Liu, W., Boehlert, C.J., Crimp, M.A., Bieler, T.R.,
16 2015. Effect of realistic 3D microstructure in crystal plasticity finite element
17 analysis of polycrystalline Ti-5Al-2.5Sn. *Int. J. Plast.* 69, 21–35.
18 <https://doi.org/10.1016/j.ijplas.2015.01.003>
- 19 Zhang, Z., Cuddihy, M.A., Dunne, F.P.E., 2015. On rate-dependent polycrystal
20 deformation: the temperature sensitivity of cold dwell fatigue. *Proc. R. Soc. A*
21 *Math. Phys. Eng. Sci.* 471, 20150214. <https://doi.org/10.1098/rspa.2015.0214>
- 22 Zhang, Z., Jun, T.S., Britton, T.B., Dunne, F.P.E., 2016. Intrinsic anisotropy of strain
23 rate sensitivity in single crystal alpha titanium. *Acta Mater.* 118, 317–330.
24 <https://doi.org/10.1016/j.actamat.2016.07.044>

- 1 Zhang, Z., Lunt, D., Abdolvand, H., Wilkinson, A.J., Preuss, M., Dunne, F.P.E., 2018.
2 Quantitative investigation of micro slip and localization in polycrystalline
3 materials under uniaxial tension. *Int. J. Plast.* 108, 88–106.
4 <https://doi.org/10.1016/j.ijplas.2018.04.014>
- 5 Zhao, Z., Ramesh, M., Raabe, D., Cuitiño, A.M., Radovitzky, R., 2008. Investigation of
6 three-dimensional aspects of grain-scale plastic surface deformation of an
7 aluminum oligocrystal. *Int. J. Plast.* 24, 2278–2297.
8 <https://doi.org/10.1016/j.ijplas.2008.01.002>
- 9 Zheng, Z., Balint, D.S., Dunne, F.P.E., 2017. Investigation of slip transfer across HCP
10 grain boundaries with application to cold dwell facet fatigue. *Acta Mater.* 127, 43–
11 53. <https://doi.org/10.1016/j.actamat.2017.01.021>
12

1 **Figures**



2

3 Fig. 1 A schematic showing the difference in the deformability of region i depending on
4 the softness of the surrounding regions. (a) The initial state and states after the
5 deformations by tensile loading (b) and (c). (b) The condition, in which region i is
6 connected to the “soft” regions in series and “hard” regions in parallel. (c) The condition,
7 in which region i is connected to the “soft” regions in parallel and “hard” regions in series.

8

9

10

11

12

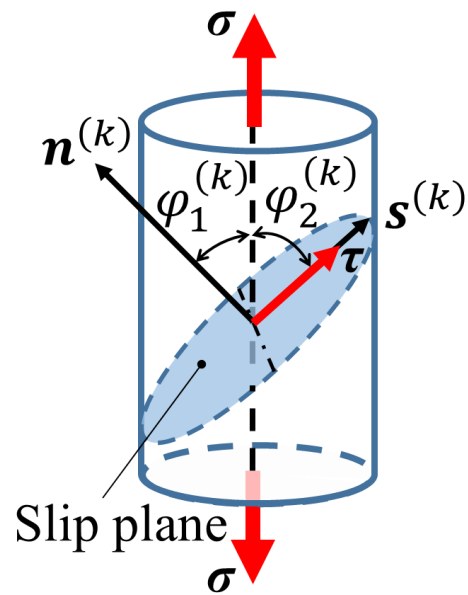
13

14

15

16

17



1

2 Fig. 2 A schematic showing the geometry of a slip system under uniaxial tensile loading.

3 \mathbf{n} is the vector normal to the slip plane and \mathbf{s} is the slip direction vector. τ is the resolved

4 shear stress (RSS) of the slip system k .

5

6

7

8

9

10

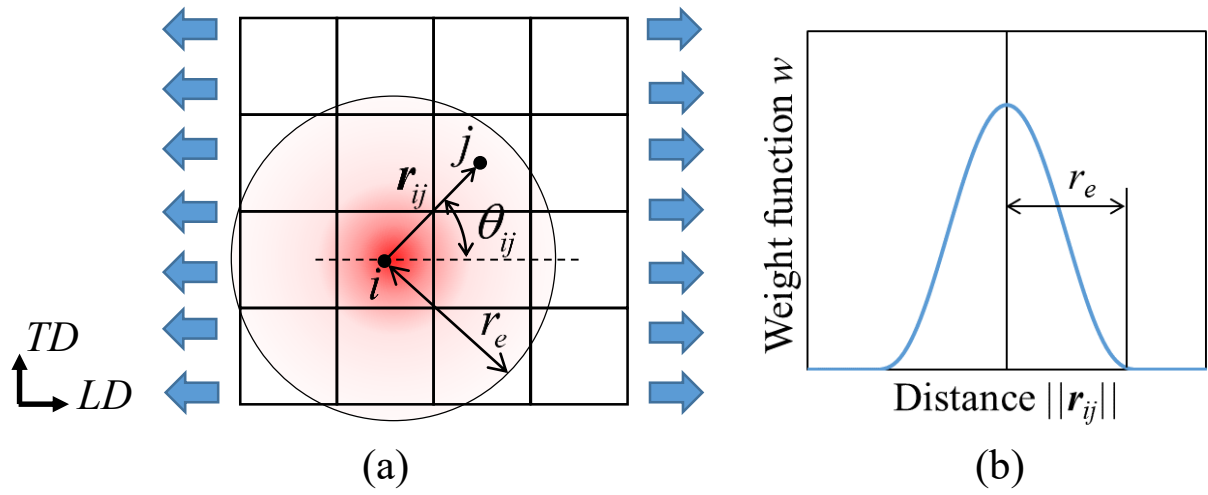
11

12

13

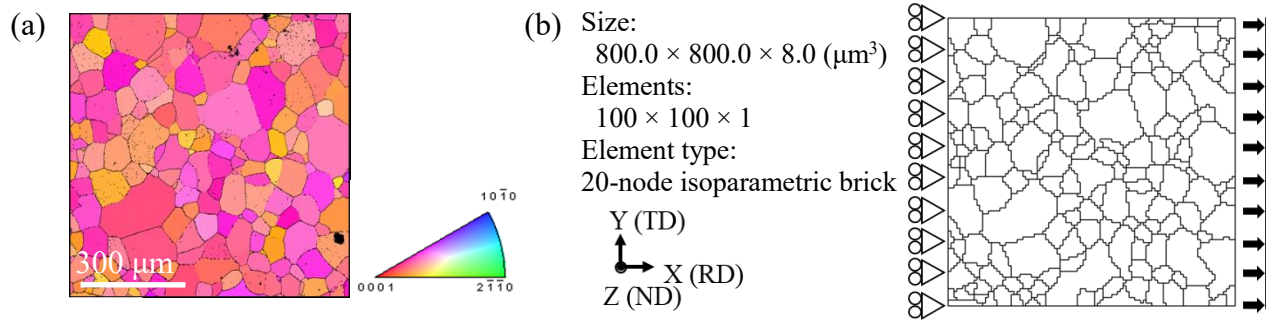
14

15



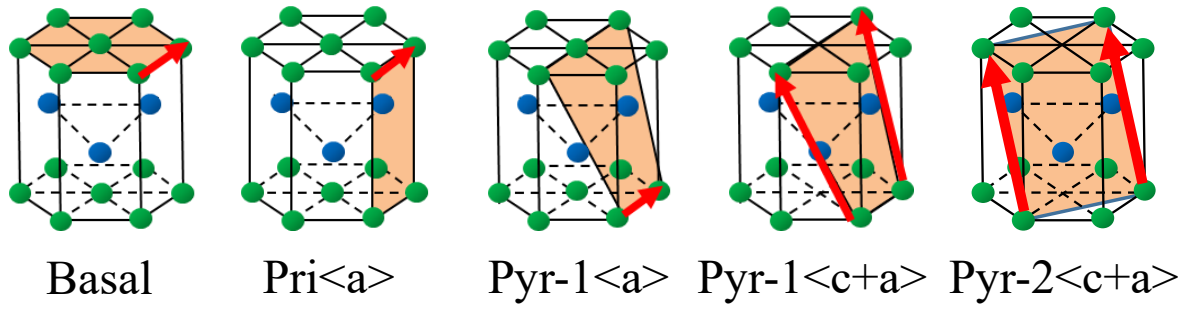
1
2
3
4
5
6
7
8
9
10
11
12
13
14
15

Fig. 3 (a) A schematic diagram showing the geometry of regions i and j . (b) A profile of the weight function to determine the interaction range.



1
2
3 Fig. 4 (a) EBSD crystal orientation map of the studied sample. (b) The geometry model
4 used for the uniaxial tensile loading analysis. The model (b) was built from the map (a)
5 using a procedure developed by Kawano et al. (2018b).

6
7
8
9
10
11
12
13
14
15
16
17
18
19
20



1

2

3 Fig. 5 Schematics showing slip systems of α -Ti. The symbols of “Basal”, “Pri<a>”, “Pyr-
 4 1<a>”, “Pyr-1<c+a>”, and “Pyr-2<c+a>” correspond to the basal slip system, prismatic
 5 <a> slip system, 1st pyramidal <a> slip system, and 1st and 2nd pyramidal <c+a> slip
 6 systems, respectively.

7

8

9

10

11

12

13

14

15

16

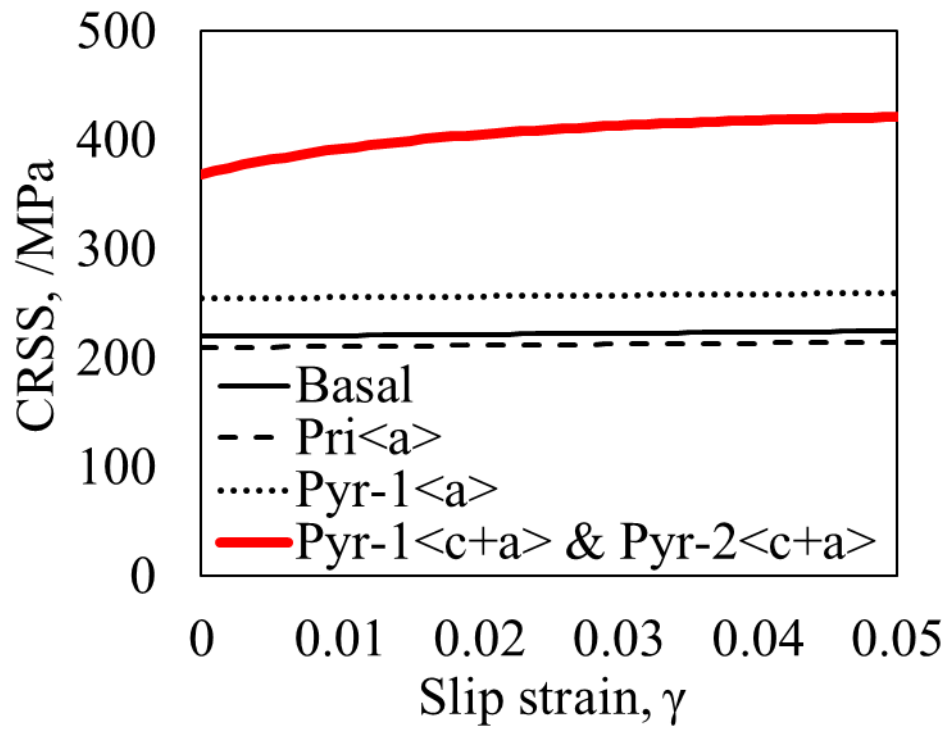
17

18

19

20

1



2

3 Fig. 6 CRSS for each slip system as a function of slip strain.

4

5

6

7

8

9

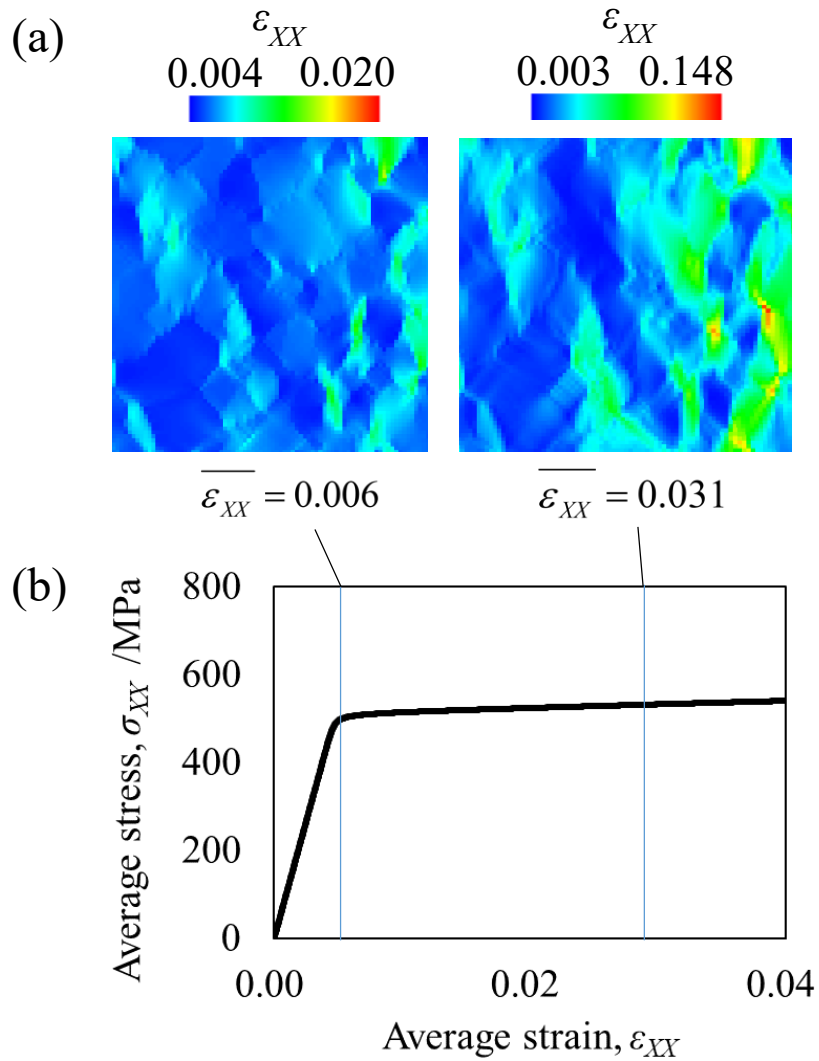
10

11

12

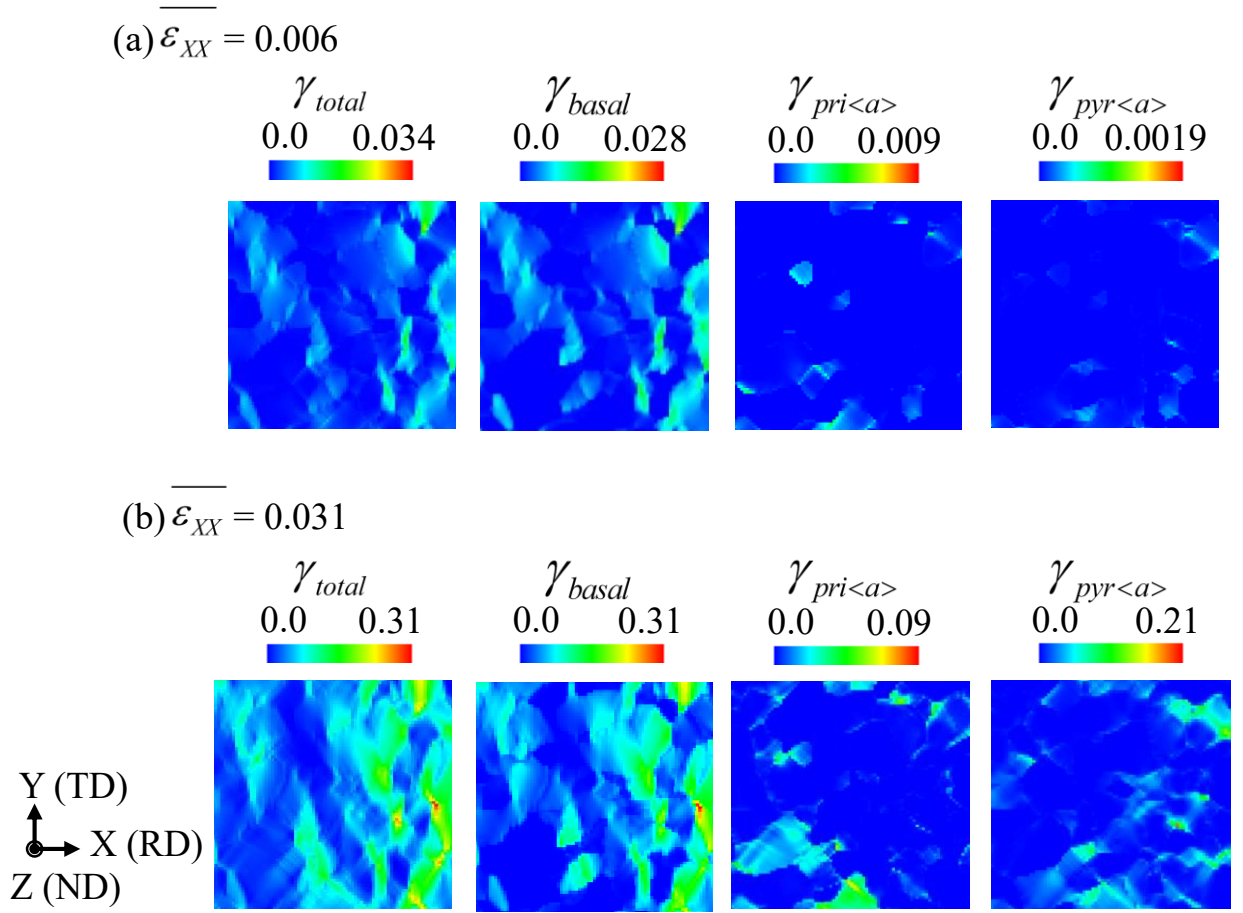
13

14



1
2
3
4
5
6
7
8
9

Fig. 7 (a) Distributions of normal strain in the X-direction. The regions 10 μm in size were removed from each side of the model as they were strongly affected by boundary conditions. (b) Profile of the stress-strain relationship.



1

2

3 Fig. 8 Distributions of slip strains γ when (a) $\overline{\varepsilon_{XX}} = 0.006$ and (b) $\overline{\varepsilon_{XX}} = 0.031$.

4 \mathcal{Y}_{basal} , $\mathcal{Y}_{pri<a>}$, and $\mathcal{Y}_{pyr<a>}$ are the summations of the absolute values of slip strains

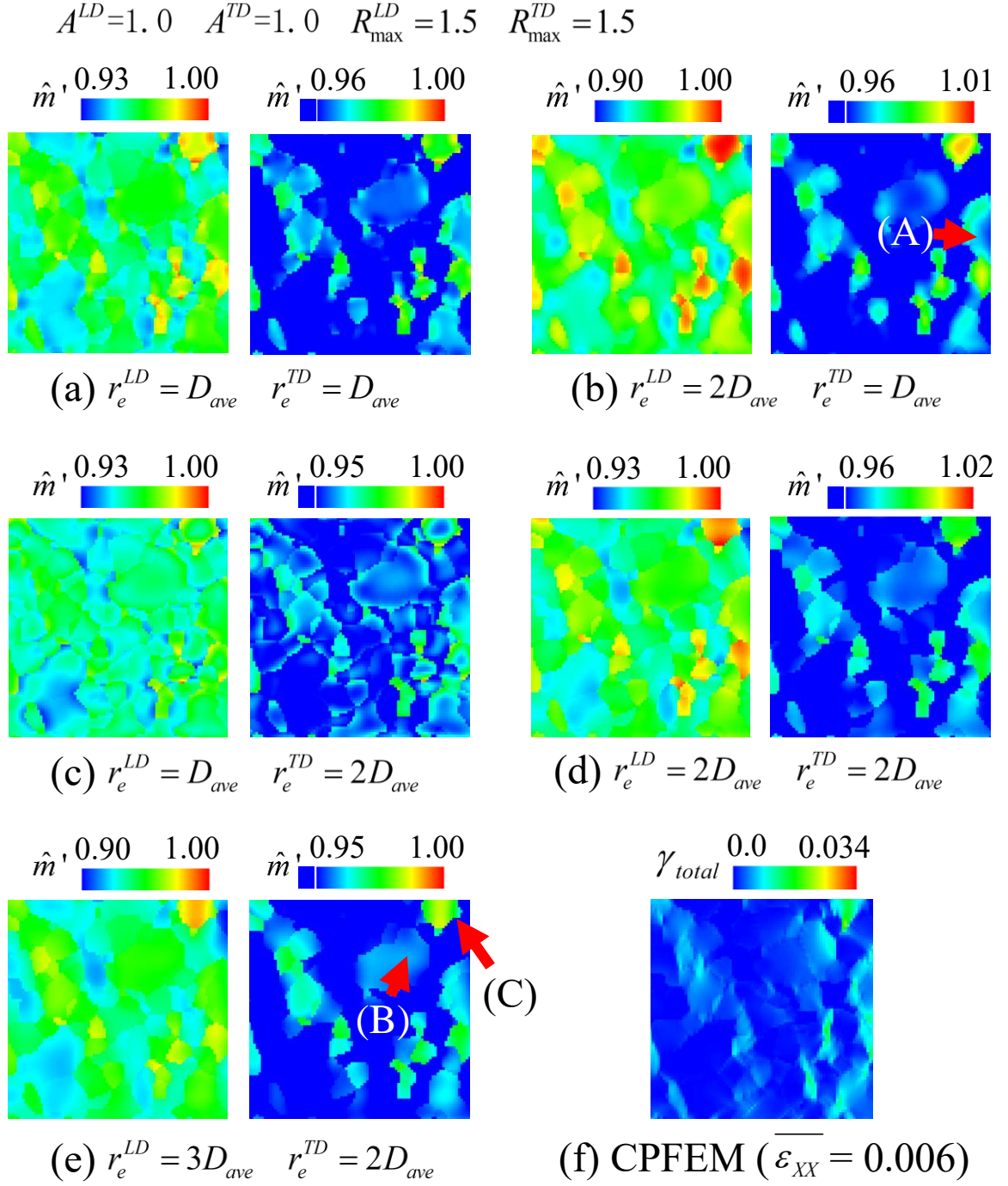
5 for the individual slip system families. The subscripts for γ refer to basal, prismatic $\langle a \rangle$,

6 and 1st pyramidal $\langle a \rangle$ slip systems, and \mathcal{Y}_{total} is the summation of \mathcal{Y}_{basal} , $\mathcal{Y}_{pri<a>}$, and

7 $\mathcal{Y}_{pyr<a>}$. The regions 10 μm in size were removed from each side of the model as they

8 were strongly affected by boundary conditions.

9



1

2

3 Fig. 9 Distributions of SOF (\hat{m}') and slip strain (γ_{total}) at the yield point obtained by the

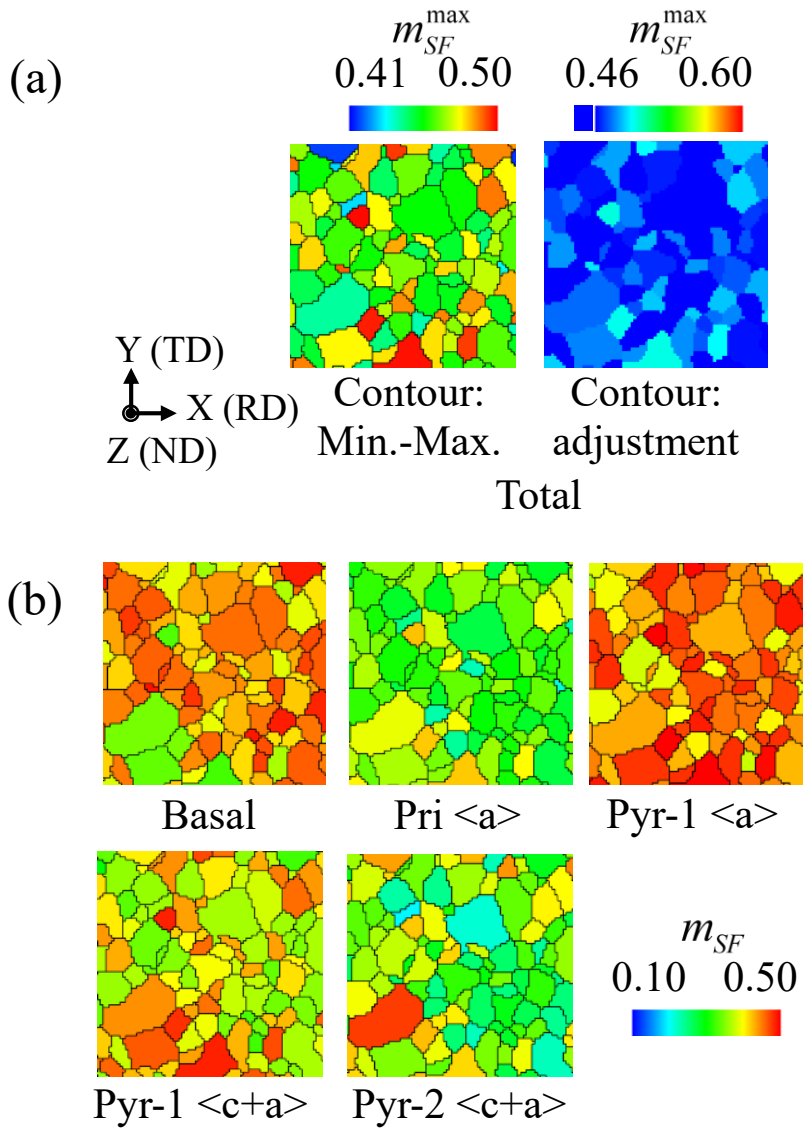
4 CPFEM analysis. (a)–(e) Changes in the distributions of \hat{m}' with the influence range r_e ,

5 whereas r_e^{LD} and r_e^{TD} represent the influence range in the loading and transverse

1 directions, respectively. The SOF distributions were obtained from the conditions (I)-(V)
2 in Table 4. D_{ave} (69.2 μm) is an average grain size. The regions 10 μm in size were
3 removed from each side of the model as they were strongly affected by boundary
4 conditions. Right-hand side figures contain the adjusted color contours to be easily
5 compared with the distribution of Fig. 9f. (f) Distributions of slip strains γ_{total} when
6 $\overline{\varepsilon_{xx}} = 0.006$.

7

8

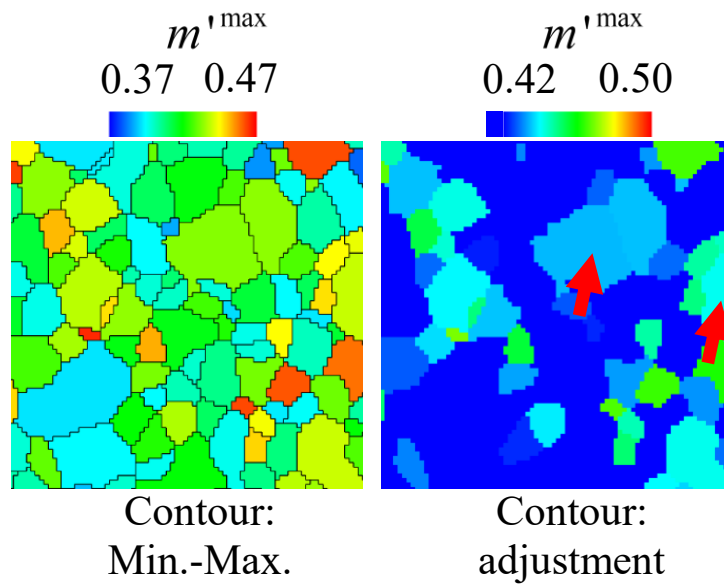


1

2

3 Fig. 10 Spatial distributions of the Schmid factor (SF) in the X-direction. (a) Spatial
 4 distributions for all of the slip systems. The right-hand side figure depicts the adjusted
 5 color contours to be easily compared with the distribution of Fig. 9(f). (b) Spatial
 6 distributions for each slip system. The regions 10 μm in size were removed from each
 7 side of the model as they were strongly affected by boundary conditions.

8



1

2 Fig. 11 Spatial distributions of the normalized Schmid factor (NSF) in the X-direction.

3 The right-hand side figure depicts the adjusted color contours to be easily compared with
 4 the distribution of Fig. 9(f). The regions 10 μm in size were removed from each side of
 5 the model as they were strongly affected by boundary conditions.

6

7

8

9

10

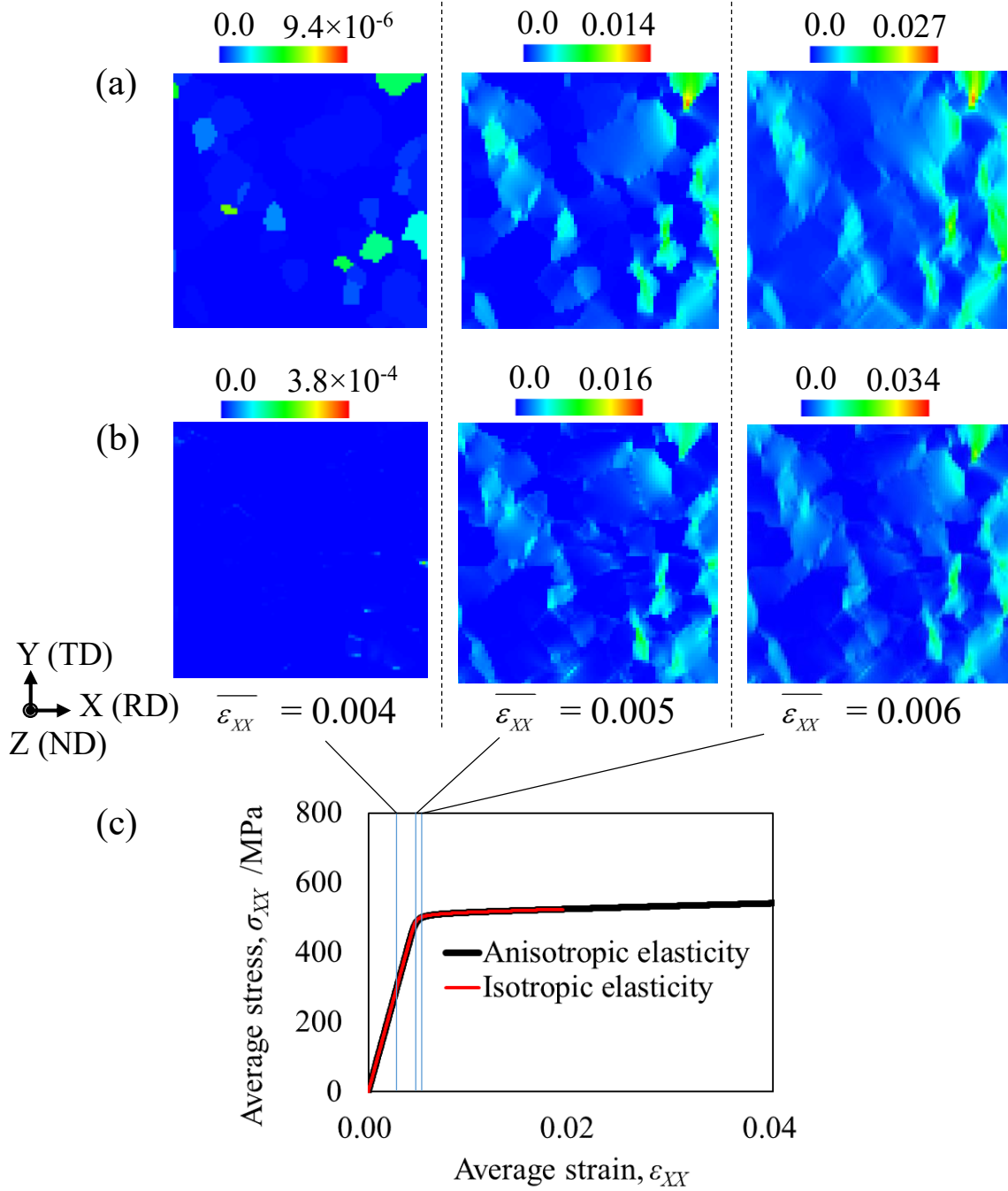
11

12

13

14

15

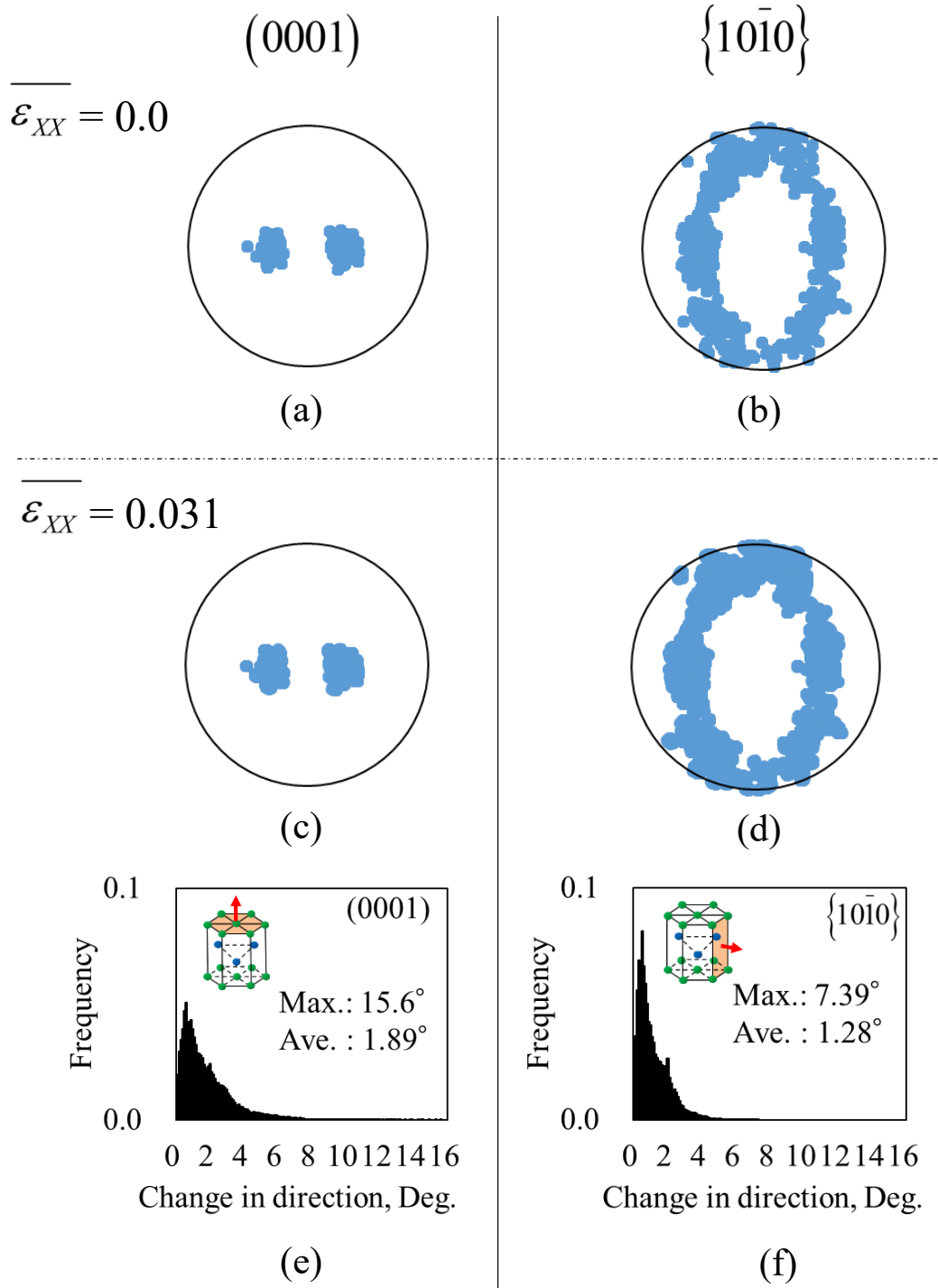


1

2 Fig. 12 (a)-(b) The distributions of γ_{total} . For (a), the γ_{total} distributions were obtained
 3 under the condition of isotropic elasticity when $E = 106.3$ GPa and $\nu = 0.34$. For (b), the
 4 γ_{total} distributions were calculated under the condition of anisotropic elasticity, a

1 condition similar to that in Fig. 9(f). The regions 10 μm in size were removed from each
2 side of the model as they were strongly affected by boundary conditions. (c) The stress–
3 strain relationship.

4
5
6
7
8
9
10
11
12
13
14
15
16
17
18
19
20
21
22



1

2

3 Fig. 13 (a) and (c) correspond to (0001) pole figures and (b) and (d) are $\{10\bar{1}0\}$ pole

4 figures when $\overline{\varepsilon_{XX}} = 0.0$ and 0.031. (e) and (f) show the relative frequency distributions

1 of change in directions of the vectors normal to the (0001) and $\{10\bar{1}1\}$ planes when

2 $\overline{\varepsilon_{xx}}$ changes from 0.0 to 0.031.

3

4

5

6

7

8

9

10

11

12

13

14

15

16

17

18

19

20

21

22

23

1 **Tables**

2

3 Table 1 Chemical composition of the sample material (wt.%).

| Ti | O | Fe |
|------|-------|-------|
| Bal. | 0.047 | 0.027 |

4

5

6 Table 2 Elastic compliance of pure titanium [(TPa)⁻¹] (Fisher and Renken, 1964).

| S_{11} | S_{12} | S_{13} | S_{33} | S_{44} |
|----------|----------|----------|----------|----------|
| 9.581 | -4.623 | -1.893 | 6.980 | 21.413 |

7

8

9

Table 3 Values used for the Voce equation [MPa].

| Slip systems | Basal | Pri<a> | Pyr-1<a> | Pyr-1<c+a> Pyr-2<c+a> |
|--------------|-------|--------|----------|--------------------------|
| τ_0 | 220.0 | 210.0 | 255.0 | 369.0 |
| τ_1 | 400.0 | 400.0 | 400.0 | 50.0 |
| θ_0 | 100.0 | 100.0 | 100.0 | 3000.0 |
| θ_1 | 200.0 | 200.0 | 200.0 | 100.0 |

10

11

12

13

14

15

16

17

- 1 Table 4 CRSS and other parameters for SOF for each condition. D_{ave} (69.2 μm) is an
 2 average grain size in the test specimen.

| Conditions | (I) | (II) | (III) | (IV) | (V) |
|------------------------------|-------------------------------------|------------|------------|------------|------------|
| CRSS | Same as τ_0 in Table 3 | | | | |
| A^{LD}, A^{TD} | $A^{LD} = A^{TD} = 1.0$ | | | | |
| $R_{max}^{LD}, R_{max}^{TD}$ | $R_{max}^{LD} = R_{max}^{TD} = 1.5$ | | | | |
| r_e^{LD} | D_{ave} | $2D_{ave}$ | D_{ave} | $2D_{ave}$ | $3D_{ave}$ |
| r_e^{TD} | D_{ave} | D_{ave} | $2D_{ave}$ | $2D_{ave}$ | $2D_{ave}$ |

3

4

5